

Journal of Geophysical Research: Solid Earth

RESEARCH ARTICLE

10.1002/2017JB014523

Key Points:

- Numerical calculation of the failure overpressure required to cause magma intrusion is dependent on pore fluid pressure
- High pore fluid pressure encourages eruptions by reducing the failure overpressure
- Different pore fluid pressure conditions can explain the difference of eruptive behavior between volcanoes

Supporting Information:

- Supporting Information S1
- Figure S1
- Data Set S1

Correspondence to:F. Albino,
fa17101@bristol.ac.uk**Citation:**

Albino, F., Amelung, F., & Gregg, P. (2018). The role of pore fluid pressure on the failure of magma reservoirs: Insights from Indonesian and Aleutian arc volcanoes. *Journal of Geophysical Research: Solid Earth*, 123.

<https://doi.org/10.1002/2017JB014523>

Received 13 JUN 2017

Accepted 29 JAN 2018

Accepted article online 6 FEB 2018

The Role of Pore Fluid Pressure on the Failure of Magma Reservoirs: Insights From Indonesian and Aleutian Arc Volcanoes

F. Albino^{1,2} , F. Amelung¹ , and P. Gregg³

¹Department of Marine Geology and Geophysics, Rosenstiel School of Marine and Atmospheric Sciences, University of Miami, Miami, FL, USA, ²School of Earth Sciences, University of Bristol, Bristol, UK, ³Department of Geology, University of Illinois at Urbana–Champaign, Champaign, IL, USA

Abstract We use numerical models to study the mechanical stability of magma reservoirs embedded in elastic host rock. We quantify the overpressure required to open tensile fractures (the failure overpressure), as a function of the depth and the size of the reservoir, the loading by the volcanic edifice, and the pore fluid pressure in the crust. We show that the pore fluid pressure is the most important parameter controlling the magnitude of the failure overpressure rather than the reservoir depth and the edifice load. Under lithostatic pore fluid pressure conditions, the failure overpressure is on the order of the rock tensile strength (a few tens of megapascals). Under zero pore fluid pressure conditions, the failure overpressure increases linearly with depth (a few hundreds of megapascals at 5 km depth). We use our models to forecast the failure displacement (the cumulative surface displacement just before an eruption) on volcanoes showing unrest: Sinabung and Agung (Indonesia) and Okmok and Westdahl (Aleutian). By comparison between our forecast and the observation, we provide valuable constraint on the pore fluid pressure conditions on the volcanic system. At Okmok, the occurrence of the 2008 eruption can be explained with a 1,000 m reservoir embedded in high pore fluid pressure, whereas the absence of eruption at Westdahl better suggests that the pore fluid pressure is much lower than lithostatic. Our finding suggests that the pore fluid pressure conditions around the reservoir may play an important role in the triggering of an eruption by encouraging or discouraging the failure of the reservoir.

1. Introduction

The past decades have provided a wealth of observations of ground surface deformation before, during, and after volcanic eruptions using Global Positioning System (GPS), tiltmeters, strainmeters, or satellite radar interferometry (InSAR). Observed preeruption inflation ranges from a few centimeters prior to the 2006 Augustine eruption, Alaska (Cervelli et al., 2006) to several meters at Sierra Negra volcano, Galapagos Islands (Geist et al., 2008). An important question for hazard assessment is whether detected inflation is a precursor for an eruption (Biggs et al., 2014; Chaussard et al., 2013; Dzurisin, 2003; Moran et al., 2011). There are many observations of preeruptive inflation at basaltic volcanoes, for example, at Krafla and Grimsvötn in Iceland (Bjornsson et al., 1979; Ewart et al., 1991; Lengliné et al., 2008; Reverso et al., 2014; Sturkell et al., 2006), Kilauea in Hawaii (Dvorak & Dzurisin, 1993), Fernandina in the Galapagos Islands (Bagnardi & Amelung, 2012), Axial Seamount in the Pacific ridge (Nooner & Chadwick, 2009), and Okmok in Alaska (Lu et al., 1998, 2010). For several andesitic and dacitic volcanoes arc-wide, InSAR surveys have documented preeruptive inflation (Chaussard & Amelung, 2012; Chaussard et al., 2013; Lu & Dzurisin, 2014; Pritchard & Simons, 2002; 2004). In contrast, other volcanic systems can show unrest in form of ground deformation, earthquakes swarms, large heat, and gas emissions for months to decades without eruption (Acciolla et al., 2015; López et al., 2012; Lowenstern et al., 2006; Martí et al., 2013; Newhall & Dzurisin, 1988). This is the case of many silicic caldera volcanoes such as Long Valley (Hill, 1984; Newman et al., 2006), Santorini (Newman et al., 2012; Parks et al., 2012), Yellowstone (Chang et al., 2007; Wicks et al., 2006), Campi Flegrei (Amoruso et al., 2007; Beauducel et al., 2004; Di Vito et al., 1999; Gottsmann et al., 2006; Lundgren et al., 2001; Orsi et al., 1999; Samsonov et al., 2014; Trasatti et al., 2008; Troise et al., 2007; Vilardo et al., 2009), or Laguna del Maule (Feigl et al., 2014; Le Mével et al., 2015).

The inflation of the ground surface in volcanic areas results from stress changes in the crust due to the accumulation of magma or the exsolution of gas inside reservoirs or due to the propagation of magma through

intrusions or conduits. Such surface displacements are often modeled at first order by analytical solutions such as point pressure sources (Mogi, 1958), finite spherical sources (McTigue, 1987), or dislocations (Okada, 1985) embedded in an elastic half-space. In a case by case approach, more realistic models based on numerical techniques have been also developed to better explain volcanic ground deformation. Such models can take into account the rheology of the crust, the heterogeneities of the rock properties and the topography of the volcano (Currenti et al., 2010; Del Negro et al., 2009; De Natale et al., 1997; Geyer & Gottsmann, 2010; Ronchin et al., 2015).

In a simplified view, the magma injection from a reservoir is "inflation predictable" (Segall, 2013), which means that an intrusion can be considered when the ground inflation reaches a critical value. Such value is related to the mechanism of failure of the magma reservoir (Burt et al., 1994; Grosfils, 2007; Gudmundsson, 1988; Pinel & Jaupart, 2000; Tait et al., 1989) and therefore will be referred to as the failure displacement in this paper. The magma reservoir, modeled as a pressurized cavity, remains intact as long as the sum of the tangential stresses affecting the reservoir's wall does not exceed the strength of the host rocks. When the magma overpressure reaches a threshold, referred to as the failure overpressure in this paper, a tensile fracture is initiated from the reservoir and the magma can propagate as a hydrofracture (Gudmundsson, 2002; Gudmundsson & Brenner, 2001; Rubin, 1995). Then, the propagation of the intrusion continues as long as the strain energy release rate exceeds the fracture toughness of the material (Gudmundsson, 2012; Kilburn, 2003; Rivalta et al., 2015).

With knowledge on the elastic properties of the overlying host rock, failure models of magma reservoirs therefore provide constraints on failure overpressure and the associated failure displacement. The influence of various parameters of the volcanic system on the tensile failure of the reservoir has been already investigated, such as the depth and the shape of the reservoir (Albino et al., 2010; Grosfils, 2007; Martí & Geyer, 2009), the mechanical properties of the host rocks (Gudmundsson, 2006; Long & Grosfils, 2009), thermal effects and host rock rheologies (Currenti & Williams, 2014; Gerbault, 2012; Gregg et al., 2012), the presence of existing structures (De Natale et al., 1997; Geyer & Martí, 2009) and surface stress perturbations induced by edifice loading (Chestler & Grosfils, 2013; Hurwitz et al., 2009; Pinel & Jaupart, 2003), flank collapse (Manconi et al., 2009; Pinel & Albino, 2013), or ice cap melting (Albino et al., 2010; Geyer & Bindeman, 2011). Moreover, depending on the pore fluid pressure (Gerbault, 2012; Grosfils et al., 2015; Gudmundsson, 2012), the failure overpressure can be of the same magnitude as the tensile strength of rock (a few to 10 MPa) (Gudmundsson, 2002, 2006; Parfitt & Wilson, 2009; Pinel & Jaupart, 2005) or be as high to exceed the confining pressure (a few tens to hundreds of megapascals) as reservoir depth increases (Grosfils, 2007; Hurwitz et al., 2009; Sammis & Julian, 1987). During a volcanic unrest, it is therefore crucial to characterize the pore fluid pressure around the magma reservoir before quantifying the failure conditions. However, the magnitude of the pore fluid pressure in volcanic systems is usually unknown (Fournier, 2007).

Several studies have examined the relationship between volcanic activity and pore fluid pressure. On the one hand, the strain changes caused by magma pressurization during a volcanic unrest affect the groundwater level. Such intuitive effect has been observed and modeled on several volcanoes such as Krafla (Iceland), Usu (Japan), and Kilauea (Hawaii) (Hurwitz & Johnston, 2003; Shibata & Akita, 2001; Stefansson, 1981; Strehlow et al., 2015). On the other hand, the change in pore fluid pressure modifies the mechanical properties of the host rocks and could therefore influence the behavior of the volcanic system. For example, Farquharson et al. (2016) conducted triaxial laboratory experiments on rock samples to show that unrest-related pore fluid pressure increase can lead to the development of fracture networks around volcanic conduits, known as pore pressure-induced embrittlement. In addition, Gressier et al. (2010) used analog models to examine how pore fluid pressure controls the emplacement of magma intrusions in sedimentary basins. They showed that an increase of pore pressure prevents the vertical propagation of magma and favors the emplacement of deep horizontal intrusions. Both works show that the pore pressure conditions can influence both the initiation and the propagation of magma intrusions.

In this paper, we investigate the failure overpressure conditions around magma reservoirs using finite element modeling. First, we perform a sensitivity study to understand the effect of pore fluid pressure and compare it to the effect of other parameters such as the depth and the radius of the reservoir or the morphology of the volcanic edifice. Then, we apply our modeling to Sinabung and Agung in Indonesia and Okmok and Westdahl in the Aleutian Islands. All these volcanic systems exhibited periods of prolonged ground inflation which at Sinabung and Okmok led to eruptions, but at Agung and Westdahl did not, highlighting the limitations of ground inflation as eruption precursor. The main objective of this study is to understand why for similar

ground inflation, some magmatic systems fail and initiate an eruption while some others remain stable without erupting. Stress threshold at which an intrusion is initiated from the magma reservoir varies between volcanoes. We will calculate for each volcano and for different pore fluid pressure conditions of this failure threshold taking into account the radius and the depth of the magma reservoir and the size of the volcanic edifice.

2. Method

2.1. Failure Criterion

The failure conditions of magma reservoirs have been investigated from the analogy of hydrofractures occurring around boreholes or tunnels (Jaeger, 1979). The approach consists to calculate stress at the wall of the cavity. Assuming that magma and host rock have the same density, the internal magma pressure P_m is equal to

$$P_m = -\rho_r g z + \Delta P_m \quad (1)$$

where ρ_r is the host rock density, g the gravitational acceleration, and z the depth from the surface (negative values). Here and in the entire study, we adopt by convention compressive stress as positive and tensile stress as negative. The first term in the equation counters the lithostatic load of the rock, creating a state of equilibrium with no deformation in the surrounding host rock. The second term, ΔP_m is an excess uniform pressure in comparison with lithostatic pressure (also referred to as overpressure), which induces host rock deformation.

For 2-D plane-strain geometry, analytical solutions of this problem have been given by Jeffery (1921) and first used to quantify the pressure required to initiate a dike intrusion from a cylindrical reservoir (Gudmundsson, 1988, 2006), considering that the dike initiates from tensile fractures (mode I). The general formulation for the tensile criterion around a sphere is given by Timoshenko et al. (1951). As we consider compressive stress as positive values, the failure criterion can be written as

$$-\sigma_t \geq (P_L - P_p + T_s) \quad (2)$$

with σ_t the tangential stress at the wall, P_L the lithostatic pressure (equal to $-\rho_r g z$), P_p the pore fluid pressure, and T_s the tensile strength of the rocks. As the medium is elastic, the tangential stress is proportional to the magma overpressure so we can introduce the ratio k , with $k = -\frac{\Delta P_m}{\sigma_t}$. Therefore, the tensile failure will be initiated when the overpressure reaches a critical value referred to as the failure overpressure, ΔP_f , and defined as

$$\Delta P_f = k(P_L - P_p + T_s) \quad (3)$$

The value of ΔP_f is dependent on the tensile strength of the rock, the pore fluid pressure conditions, and the lithostatic pressure. The tensile strength of rocks can be measured by uniaxial tensile testing of natural samples. From such experiments, Touloukian et al. (1981) report tensile strengths of 13.8 ± 2.1 MPa for granite and 8.6 ± 1.4 MPa for pristine basalt. However, these values have to be considered as upper limits because crustal processes such as faulting, fracturing, or hydrothermal activity reduces the tensile strength (Schultz, 1995). For example, in situ measurements in Iceland provide strength values of 1–6 MPa (Haimson & Rummel, 1982). Throughout the paper, we will use a constant value of 10 MPa for T_s and we will be aware that the failure overpressure calculated would correspond to an upper bound.

There are different approaches to include the pore fluid pressure conditions in models for reservoir failure (Gerbault, 2012; Grosfils et al., 2015; Gudmundsson, 2012). A common approach considers that some fluids are present in the rock adjacent to the reservoir (Lister & Kerr, 1991; McLeod & Tait, 1999; Rubin, 1995). In that case, the pore fluid pressure equals the lithostatic pressure ($P_p = P_L$) and the failure overpressure is of the magnitude of the tensile strength, $\Delta P_f = kT_s$ (e.g., Gudmundsson, 2002, 2006; Parfitt & Wilson, 2009; Pinel & Jaupart, 2005). An alternative approach considers that preexisting fluids are negligible at the contact between the reservoir and the host rock. In that way, there is zero pore fluid pressure ($P_p = 0$) and the failure overpressure becomes strongly dependent on the lithostatic stress $\Delta P_f = k(P_L + T_s)$ (Grosfils, 2007; Sammis & Julian, 1987). For zero pore fluid pressure, the failure overpressure for a reservoir at 10 km depth will be almost twice larger than that for a reservoir at 5 km depth.

The solution of ΔP_f is well known for a spherical reservoir embedded in an infinite space, in which the ratio k is constant along the wall and equal to 2 (Jaeger, 1979; Tait et al., 1989). However, for more complex geometries

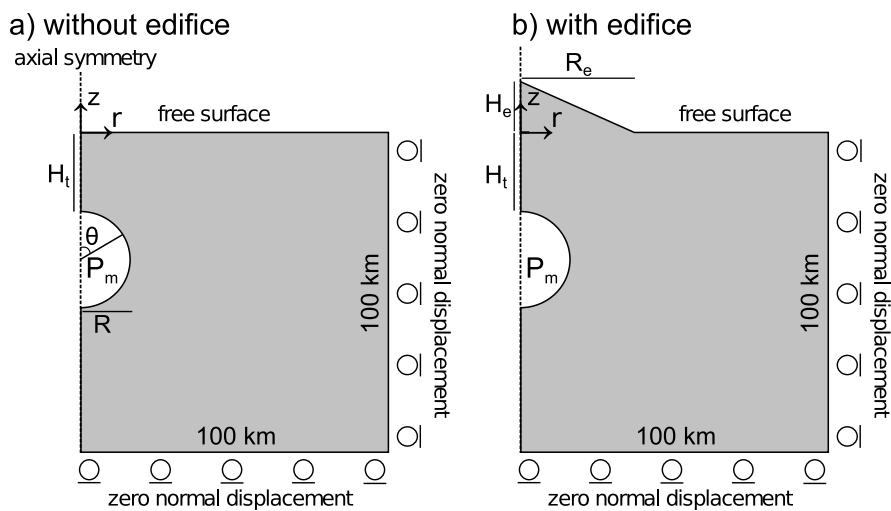


Figure 1. Mechanical model used to calculate the failure overpressure required to initiate an intrusion: (a) without edifice and (b) with edifice. In Figure 1a the stress field is lithostatic with $\sigma_r = \sigma_{\text{phi}} = \sigma_z = P_L$. In Figure 1b the initial lithostatic stress field is modified by the edifice loading. $\sigma_z > \sigma_r = \sigma_{\text{phi}}$ with $\sigma_z = P_L + (\rho_r g H_e) \frac{R_e - r}{H_e}$ below the edifice.

and/or nonlithostatic stress field, the ratio k cannot be easily determined and numerical models are therefore required to assess the failure conditions.

2.2. Finite Element Modeling

Stress and strain are numerically calculated solving the equations for linear elasticity with the Finite Element Method (FEM), using the software COMSOL MULTIPHYSICS (<https://www.comsol.com>). The geometry of the mechanical model is a 2-D axisymmetrical box of 100×100 km, with a mesh of about 10,000 triangular elements that is refined around the volcanic edifice and the magma reservoir. The width and the height of the box are located far enough from the magma reservoir to limit the influence of boundaries on the stress calculation. A condition of no displacement in the normal direction is fixed to the right and bottom boundaries. The top boundary corresponds to the surface and is free to move, and the left boundary is the axis of symmetry (Figure 1). We consider homogeneous and isotropic elastic host rock, characterized by its shear modulus G and its Poisson's ratio ν .

In the absence of tectonic stress, the initial state in numerical models is assumed to be either a lithostatic stress field ($\sigma_r = \sigma_{\phi} = \sigma_z = P_L$) or a vertical uniaxial strain ($\sigma_r = \sigma_{\phi} = \frac{\nu}{1-\nu} \sigma_z$) (e.g., Currenti & Williams, 2014; Grosfils, 2007; Sartoris et al., 1990). In our study, we assume the initial stress as lithostatic (e.g., no deviatoric stress), which is considered as the most likely state of stress (e.g., McGarr, 1988), especially for mature portion of the crust where different processes such as deformation, faulting, or fracturing tend to reduce deviatoric stresses. To model this state of stress, we therefore impose on each element of the host rock an internal body load per volume, $\rho_r g$ and a preexisting lithostatic stress.

The first set of models reproduces the simplest case of a magma reservoir embedded in a lithostatic stress field (Figure 1a). The magma reservoir is modeled as a half spherical cavity with a radius R and a top depth H_t (depth considered as negative values). Total pressure inside the magma reservoir, P_m , is applied as a normal stress at the reservoir wall. It is composed of a depth-dependent component, $-\rho_r g z$, which compensates the weight of the surrounding rock and a uniform overpressure, ΔP_m , which could be induced by different processes such as magma replenishment, volatile exsolution, or fractional crystallization. When ΔP_m is set to zero, the magmatic reservoir is in a stress equilibrium with the surrounding medium and no deformation is generated.

The second set of models takes into account the effect of the load of the volcanic edifice. The edifice is modeled as a cone, characterized by a radius R_e and a height H_e (Figure 1b). In that model, the top depth of the reservoir H_t is now calculated from the base of the edifice. The edifice is imposed as a body loaded volume without initial prestress. Below the edifice, the initial conditions (prestress and loading) are set the same as in the previous model. The edifice load will modify the initial lithostatic stress field and induce deformation in the crust beneath. This configuration simulates the case where the construction of an edifice is more rapid

Table 1
Model Parameters and Variables

	Description/Unit	Value
Parameters		
ν	Poisson's ratio	0.25
T_s	Tensile strength (MPa)	10
ρ_r	Rock density (kg.m^{-3})	2,800
g	Constant gravity (m.s^{-2})	9.81
Variables		
R	Reservoir radius (m)	
H_t	Reservoir top depth (m)	
H_c	Reservoir center depth (m)	
R_e	Edifice radius (m)	
H_e	Edifice height (m)	
G	Shear modulus (GPa)	

than the timescale required to reach stress equilibrium. Parameters and variables used in our modeling are reported in Table 1.

Failure overpressures are calculated numerically using the tensile failure criterion described in section 2.1. As the failure conditions now vary along the wall of the reservoir, equation (3) can be rewritten as

$$\Delta P(\theta) = k(\theta)(P_L(\theta) - P_p(\theta) + T_s) \quad (4)$$

where θ is the angle between the location at the wall and the vertical axis (Figure 1), and the function $k(\theta)$, the ratio between the magma overpressure applied in the model and the induced tangential stress at the reservoir's wall. Because the crust rheology is elastic, only one model run is needed to calculate numerically the function $k(\theta)$. This function is minimum at the location $\theta = \theta_f$, where θ_f corresponds to the failure location. By using θ_f in equation (4), we can estimate the magma overpressure required to cause the reservoir failure $\Delta P_f = \Delta P(\theta_f)$.

For the case with edifice loading, we require two model runs: (1) a model without edifice loading but with reservoir overpressure (previous case) and (2) a model with edifice loading but without reservoir overpressure ($P_m = P_L$). Based on the superposition principle previously used in Pinel and Jaupart (2003) and Albino et al. (2010), we are able to calculate the overpressure required for failure below an edifice through the following function:

$$\Delta P(\theta) = k(\theta)(\sigma_{t_e}(\theta) - P_p(\theta) + T_s) \quad (5)$$

where σ_{t_e} is the total tangential stress at the reservoir wall, which is composed of the preedifice lithostatic stress P_L and the stress induced by the edifice loading. For each model, we take into account the two different pore fluid pressure conditions discussed previously: zero pore pressure where $P_p(\theta) = 0$ and lithostatic pore pressure where $P_p(\theta) = P_L(\theta)$. For simplicity, we assume that pore pressure conditions are not affected by the edifice. This assumption is valid considering that (1) pore fluid pressure changes induced by the elastic load are fully dissipated at present time and (2) the water table does not significantly change during the construction of the edifice.

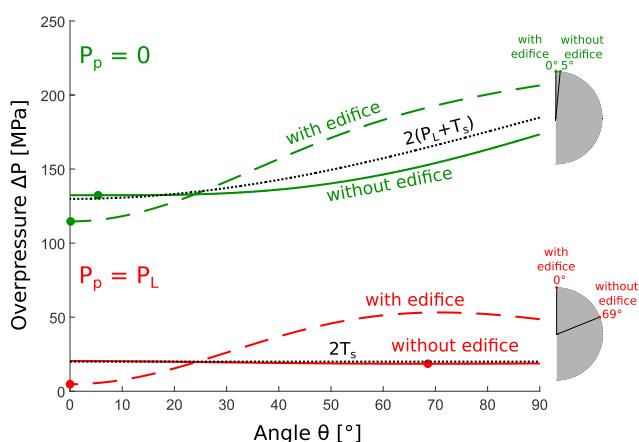


Figure 2. Overpressure required to initiate tensile fractures as a function of the angle θ in the case of a spherical reservoir ($R = 1,000$ m, $H_t = -2,000$ m) for zero pore fluid pressure (green lines) and lithostatic pore fluid pressure (red lines). Solid lines = without edifice; dashed lines = with conical edifice ($R_e = 3,000$ m, $H_e = 1,250$ m). Here we assume $T_s = 10$ MPa and $\rho_r = 2,800$ kg.m^{-3} ; dotted black lines = analytical solutions $2(P_L + T_s)$ and $2T_s$. For each model, the failure overpressure ΔP_f is the local minimum showed by the dots. The location of the angle of failure, θ_f , for the different cases are reported on the right sketch.

Figure 2 details how the failure overpressure is calculated at the reservoir's wall for the two pore fluid pressure cases. Solid and dashed colored lines correspond to the case without edifice and with edifice, respectively. For each case, the minimum of the function $\Delta P(\theta)$ is shown by a dot, which indicates the failure overpressure, ΔP_f , and the angle of failure, θ_f . For the zero pore fluid pressure without edifice, the failure occurs at $\theta_f = 5^\circ$ with $\Delta P_f = 132.3$ MPa. This is in good accordance with Grosfils (2007), who found that for his corresponding case, the failure occurs at the top (equivalent to $\theta_f = 0^\circ$) for a normalized overpressure of 2 (equivalent to $\Delta P_f = 2(P_L + T_s) = 129.9$ MPa) (see their Figures 7b and 10b for details).

For the lithostatic pore fluid pressure without edifice, the failure occurs at $\theta_f = 69^\circ$ with $\Delta P_f = 18.6$ MPa. The failure location found is in accordance with the value of 70.5° deduced from the analytical solution $\text{acos}(\frac{R}{|H_c|})$ given by Jeffery (1921) and McTigue (1987) (H_c being the center depth of the reservoir). This location corresponds to the point of tangency where the line must be tangent to the reservoir's wall and intersects the free surface at the vertical axis.

For the edifice model, $\Delta P_f = 114.7$ MPa and $\theta_f = 0^\circ$ in the case of zero-fluid pore pressure, and $\Delta P_f = 4.8$ MPa and $\theta_f = 0^\circ$ if pore fluid pressure is considered lithostatic. The loading of the edifice focuses the failure at the top of the spherical reservoir, as already suggested by Pinel and Jaupart (2003), Grosfils (2007), and Hurwitz et al. (2009). Moreover, it is interesting to notice

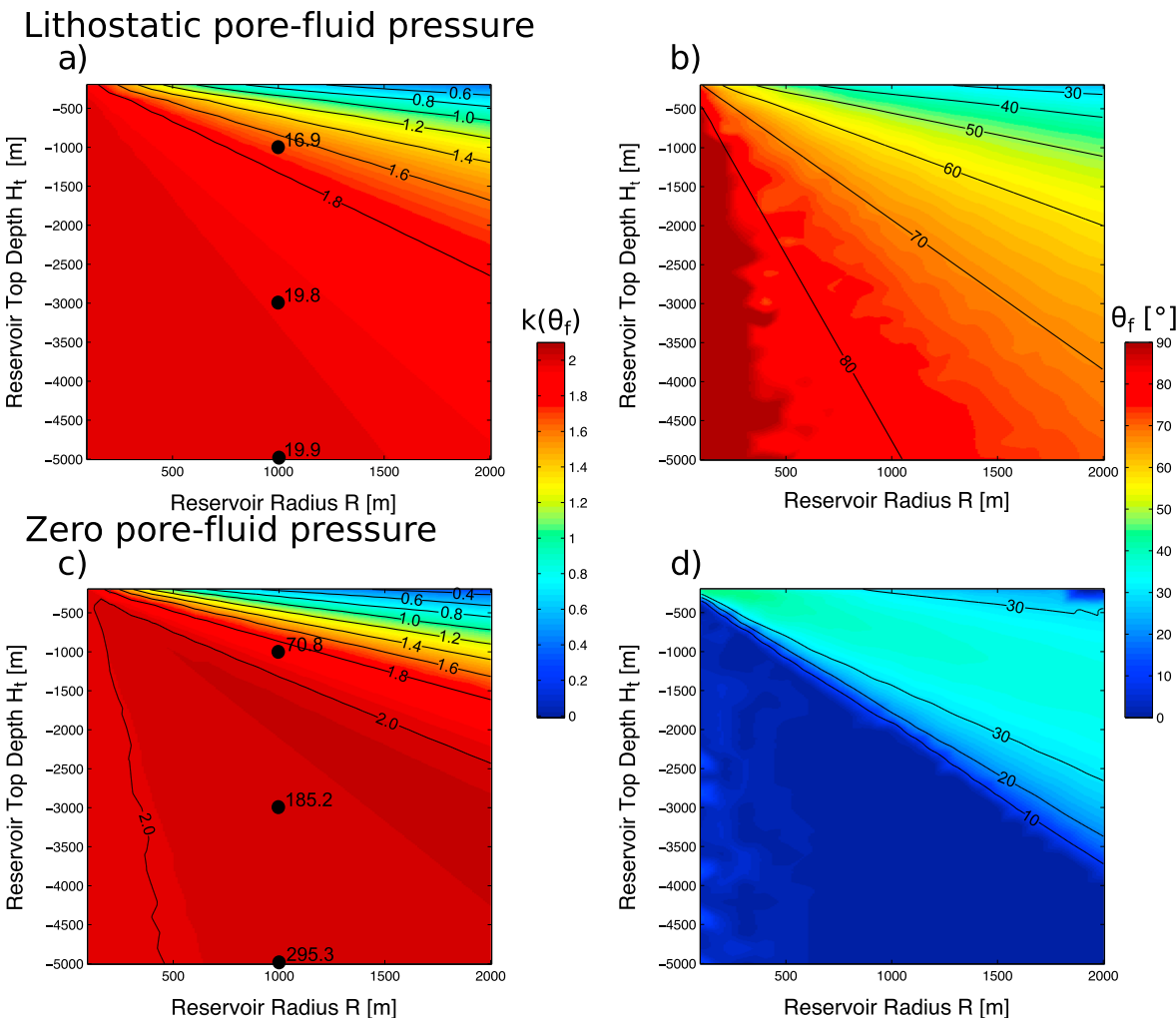


Figure 3. Normalized failure overpressure $k(\theta_f)$ (left) and location of the failure at the wall θ_f (right), as function of the radius and the top depth of a spherical reservoir embedded in an elastic half-space subject to a lithostatic stress field (Figure 1a) for (a,b) lithostatic pore fluid pressure and (c,d) zero pore fluid pressure. Numbers are nonnormalized overpressure values ΔP_f , for $R = 1,000$ m and $H_t = [-1,000 \text{--} -3,000 \text{--} -5,000]$ m, using $T_s = 10$ MPa and $\rho_r = 2,800 \text{ kg.m}^{-3}$.

that for both pore pressure conditions, the decrease of the failure overpressure induced by the edifice load is identical and about 15 MPa.

Based on this approach, we perform a parametric study by using three different model configurations. For the first configuration, the magma reservoir is embedded in an elastic half-space with lithostatic stress field (Figure 3). The second model configuration (topographic loading model, Figure 4) includes the loading stress induced by a conical volcanic edifice. For these two configurations, the radius and the top depth of the reservoir vary. In the third model configuration (Figure 5), the radius and the top depth of the reservoir are kept constant but the edifice size varies.

3. Modeling Results

3.1. Effect of the Radius and the Depth of the Reservoir

To compare the results between the two pore fluid pressure conditions, the failure overpressures are normalized by the term $(P_L(\theta_f) - P_p(\theta_f) + T_s)$. From equation (4), the normalized failure overpressure corresponds to the value $k(\theta_f)$. Figure 3 shows $k(\theta_f)$ and θ_f obtained in a lithostatic stress field for lithostatic pore fluid pressure (Figures 3a and 3b) and zero pore fluid pressure (Figures 3c and 3d). The reservoir radius and the reservoir top depth range from 100 to 2,000 m and from -200 to $-5,000$ m, respectively. Using step sizes of 100 m and 200 m, respectively, we conduct 500 model runs.

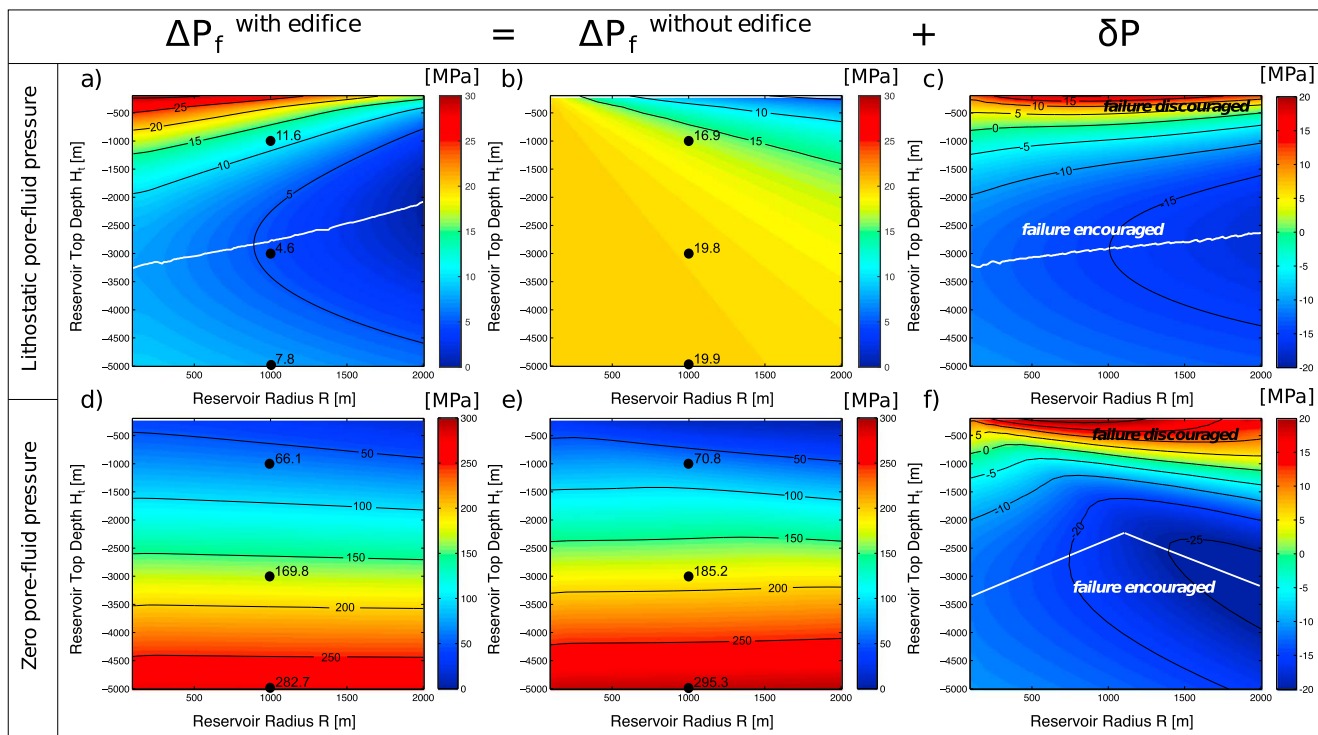


Figure 4. Failure overpressure considering the topographic loading of a fixed edifice ($R_e = 5,000$ m and $H_e = 1,250$ m). The final ΔP_f is a summation of the previous failure overpressure without edifice (Figure 3) and a term δP . Calculation is done for lithostatic pore fluid pressure (a–c) and for zero pore fluid pressure (d–f). White lines indicate depths where ΔP_f and δP are minimum.

In both cases, the normalized failure overpressure increases with increasing reservoir depth and with decreasing reservoir radius. For the lithostatic case, normalized values range from 0.4 for large and shallow reservoirs ($R = 2,000$ m, $H_t = -200$ m) to 2 for small and deep reservoirs ($R = 100$ m, $H_t = -5,000$ m). For a reservoir radius of 1,000 m, the failure overpressure increases from 16.9 MPa at 1 km depth to 19.9 MPa at 5 km depth, using $T_s = 10$ MPa (Figure 3a). For the zero pore fluid pressure case, normalized values range in the same order of magnitude from 0.25 to 2, according to reservoir depth. However, in that case, the failure overpressures are much higher than in the lithostatic pore fluid pressure case. For the reservoir radius of 1,000 m, the failure overpressure changes from 70.8 MPa to 295.3 MPa from 1 to 5 km depth, using $\rho_r = 2,800 \text{ kg.m}^{-3}$ (Figure 3c). The failure overpressure increases with depth by only 15% in the lithostatic case and by 75% in the zero pore fluid pressure case. With zero pore fluid pressure around the reservoir, the conditions of failure are strongly depth dependent and would require large overpressures to initiate an eruption.

Another difference between the two pore fluid pressure assumptions is the location of the failure (Figures 3b and 3d). For lithostatic pore fluid pressure, the location of the failure for a spherical reservoir is a function of the radius and the depth of the reservoir, with $\theta_f = a \cos(\frac{R}{|H_t|+h})$. For top depth deeper than 1 km, the failure will occur at the periphery of the reservoir $\theta_f > 45^\circ$ (Figure 3b). At the failure point, the direction of propagation is given by the maximum compressive stress, which is radial from the reservoir's wall. Under lithostatic pore pressure, the failure will favor the emplacement of subhorizontal intrusions. Under zero pore fluid pressure, the failure occurs at the top of the reservoir for most of the cases ($\theta_f = 0$) and deviates at only 30–40° from the pole for shallow reservoirs (Figure 3d). Such pore pressure conditions will therefore favor the initiation of subvertical intrusions.

3.2. Effect of the Edifice Loading

Figure 4 shows the failure overpressure for the two pore fluid pressure assumptions in the second model configuration, taking into account the load of the volcanic edifice (Figure 1b). As we consider elastic rheology, the failure overpressure below a volcanic edifice (Figures 4a and 4d) is the sum of the failure pressure in a lithostatic stress field (Figures 4b and 4e) and a term, δP , reflecting the effect of the loading stress due to the edifice (Figures 4c and 4f). Positive (negative) δP indicates that the edifice loading prevents (enhances) failure.

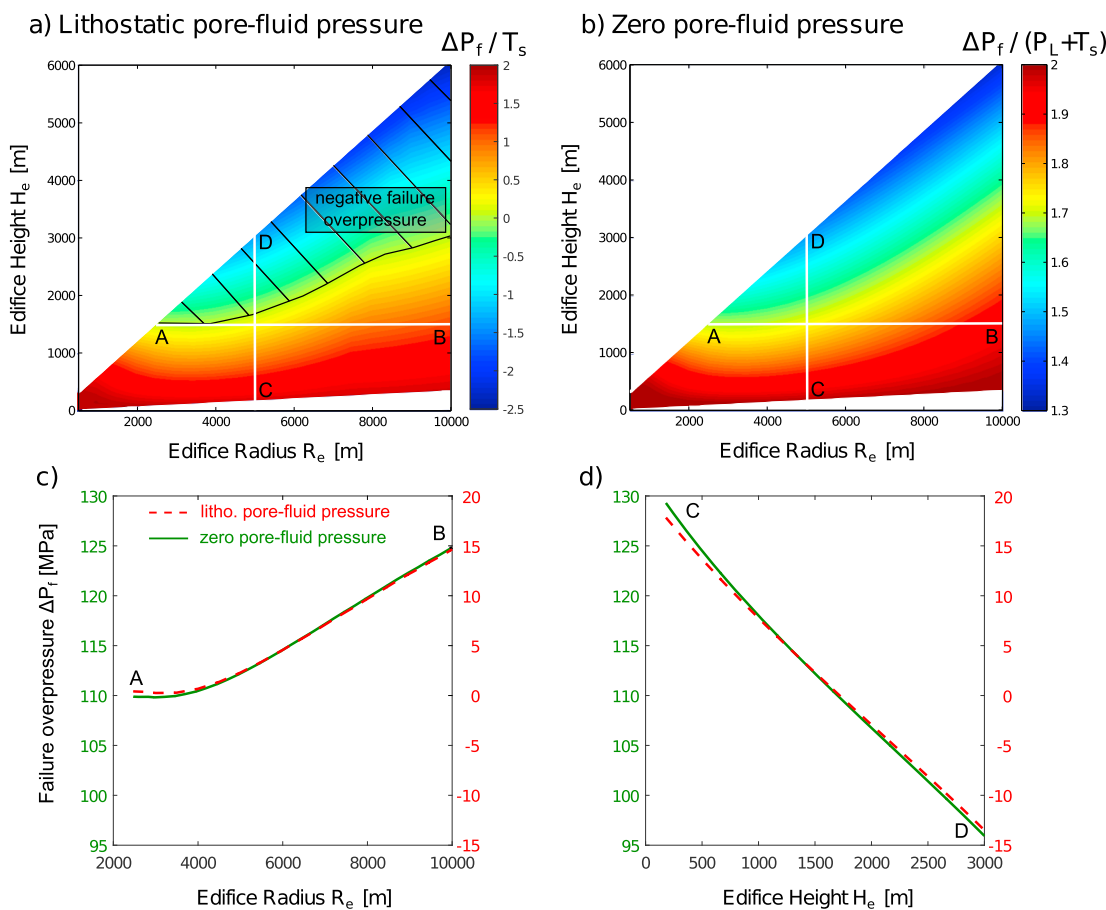


Figure 5. Normalized failure overpressure of the reservoir as a function of the radius and the height of the edifice for a spherical magma reservoir ($R = 1,000$ m, $H_t = -2,000$ m) for (a) lithostatic pore fluid pressure and (b) zero pore fluid pressure. (c, d) The profiles A-B and C-D show ΔP_f as a function of R_e ($H_e = 1,500$ m) and H_e ($R_e = 5,000$ m), respectively.

For the lithostatic pore fluid pressure case, the failure overpressure is highest for small reservoirs located at shallow depth (Figure 4a). For increasing reservoir depth, ΔP_f decreases until a minimum is reached at intermediate depth between $-2,000$ m and $-3,000$ m below the base of the cone (white line in Figure 4a). For the zero pore fluid pressure case, the failure overpressure is still largely dependent on the depth of the reservoir (Figure 4d).

However, the variation of failure overpressure due to edifice loading, δP , is similar in both cases (Figures 4c and 4f). The edifice loading discourages the failure for reservoirs shallower than 1,000 m and encourages failure of reservoirs at greater depth. For $H_t = -200$ m, the failure overpressure increases by about 22 MPa for both pore fluid pressure cases. In contrast, for $H_t = -3,000$ m, the failure overpressure decreases by 15 MPa in both cases. The change is due to the transition of the horizontal normal stress induced by the edifice loading to the reservoir's wall from compressive regime at shallow depth to tensile regime at deep depth (Pinel & Jaupart, 2003, 2004). For both pore fluid pressure conditions, the largest decrease in failure overpressure occurs for reservoirs located around 3,000 m depth (white line in Figures 4c and 4f).

In the third model configuration, the size and the depth of the reservoir are kept constant, but the edifice size varies. Edifice radius R_e ranges from 500 to 10,000 m, with a step size of 500 m and edifice slope θ_e from 2 to 30° , with a step size of 2° . The normalized failure overpressures are shown in Figures 5a and 5b as a function of the radius and height of the edifice, for the two pore fluid pressure assumptions. In both cases, the failure overpressure increases with increasing edifice radius and decreases with increasing edifice height. With the load of the edifice, the failure occurs at the top of the reservoir for both pore fluid pressure conditions, which will favor the initiation of subvertical intrusions leading eventually to summit eruptions. In the case of lithostatic pore fluid pressure, there are negative failure overpressures for large edifice heights (Figure 5a),

which means that the reservoir is not mechanically viable under such edifices. Although the amplitude of the failure overpressure is different between the two pore fluid conditions, we notice that the patterns are the same (Figures 5c and 5d). Variations are mostly linear with +2.5 MPa/km for the radius (Figure 5c) and -12 MPa/km for the height (Figure 5d). These results underline that the failure overpressure changes due to stress perturbations are independent of the conditions of pore fluid pressure around the reservoir.

4. Application of Failure Models to Sinabung, Agung, Westdahl, and Okmok Volcanoes

In this section, we apply our failure models to real volcanoes. We select two pairs of volcanoes: Sinabung and Agung in Indonesia and Okmok and Westdahl in the Aleutian. The pair selection is based on the following characteristics: (1) both volcanoes showed sign of unrest, at one volcano the unrest is followed by an eruption but not at the other one; (2) eruptions are initiated by magma intrusions from a reservoir as a result of rock fracturing, and our mechanical models apply; (3) volcanoes are close enough in space to have similar geological and tectonic settings.

We calculate the failure overpressure, taking into account the reservoir depth and the loading stress of the edifice. We investigate the failure overpressure considering lithostatic pore fluid pressure ($P_p = P_L$) and zero pore fluid pressure ($P_p = 0$). With assumptions on the shear modulus, we then convert the failure overpressure to failure displacement, which corresponds to the maximum vertical surface displacement expected before the failure of the reservoir. The total ground displacements in our FEM model are the sum of two components: (i) subsidence by a few meters related to the implementation of the surface load and (ii) inflation caused by the pressurization of the reservoir. With an elastic assumption, the subsidence occurs immediately or over a short period of time after the occurrence of the surface load. For the calculation of our failure displacements, we do not consider this subsidence but only displacements related to the reservoir pressurization.

4.1. Eruptions and Ground Deformation

4.1.1. Example 1: Sinabung and Agung

Sinabung and Agung are located in the Indonesian subduction arc and are both associated with a strike-slip setting (Acocella & Funiciello, 2010; Chaussard & Amelung, 2014; Hughes & Mahood, 2011). Sinabung is a 2,460 m high andesitic-dacitic stratovolcano in northern Sumatra (Indonesia), 25 km north of Toba caldera (Figure 6a, top). Edifice flanks are composed of successive lava flows (Global Volcanism Program, 2013), which indicates past nonexplosive eruption episodes. On 27 August 2010, Sinabung erupted after a period of steady inflation, producing a 5 km high Plinian ash cloud above the summit. A cumulative displacement of about 10 cm in line-of-sight (LOS) direction was detected by InSAR during 3.5 years preceding the eruption (Chaussard & Amelung, 2012; Chaussard et al., 2013). The 2010 phreatic episode was the first eruption in modern times, except possibly an unconfirmed eruption in 1881 (Sutawidjaja et al., 2013).

The 3,000 m high Agung stratovolcano in Bali is built on the caldera rim of neighboring Batur volcano (Figure 6a, top). Three eruptions were reported during the last two centuries, in 1808, 1843, and 1963–1964. The latter was one of the largest eruptions of the twentieth century and produced voluminous ashfall, pyroclastic flows, and lahars, killing a total of 1,138 people (Witham, 2005). Between mid-2007 and 2009, Agung inflated by more than 13 cm in LOS direction but did not erupt (Chaussard & Amelung, 2012; Chaussard et al., 2013). Quiescence over decades to centuries indicates the lack of permanent conduits to transport the magma to the surface at Sinabung and Agung in contrast to persistently active volcanoes (e.g., Soufrière Hills, Popocatepetl, or Merapi). An eruption would be initiated by fracturing a new path into the crust.

4.1.2. Example 2: Okmok and Westdahl

The two volcanoes are located at 260 km distance in the Aleutian subduction arc in similar tectonic settings (Acocella & Funiciello, 2010; Chaussard & Amelung, 2014; Hughes & Mahood, 2011; Zellmer, 2008). Okmok, a basaltic shield volcano (500 m) located on Umnak Island in the Aleutian arc (Figure 6a, bottom), is one of the most active Aleutian volcanoes with 11 known eruptions since 1900 (Global Volcanism Program, 2013). The summit is composed of two overlapping 10 km wide calderas formed about 12,000 and 2,050 years ago (Larsen et al., 2007). Subsequently, numerous small satellite cones and lava domes have developed on the caldera floor (Byers, 1959). The more recent cones are basaltic and formed after the disappearance of a caldera lake. Intense hydrothermal activity with fumaroles and hot springs is often observed within the caldera. Historical eruptions have produced lava flows from the edge of the caldera rim. Between the last two eruptions

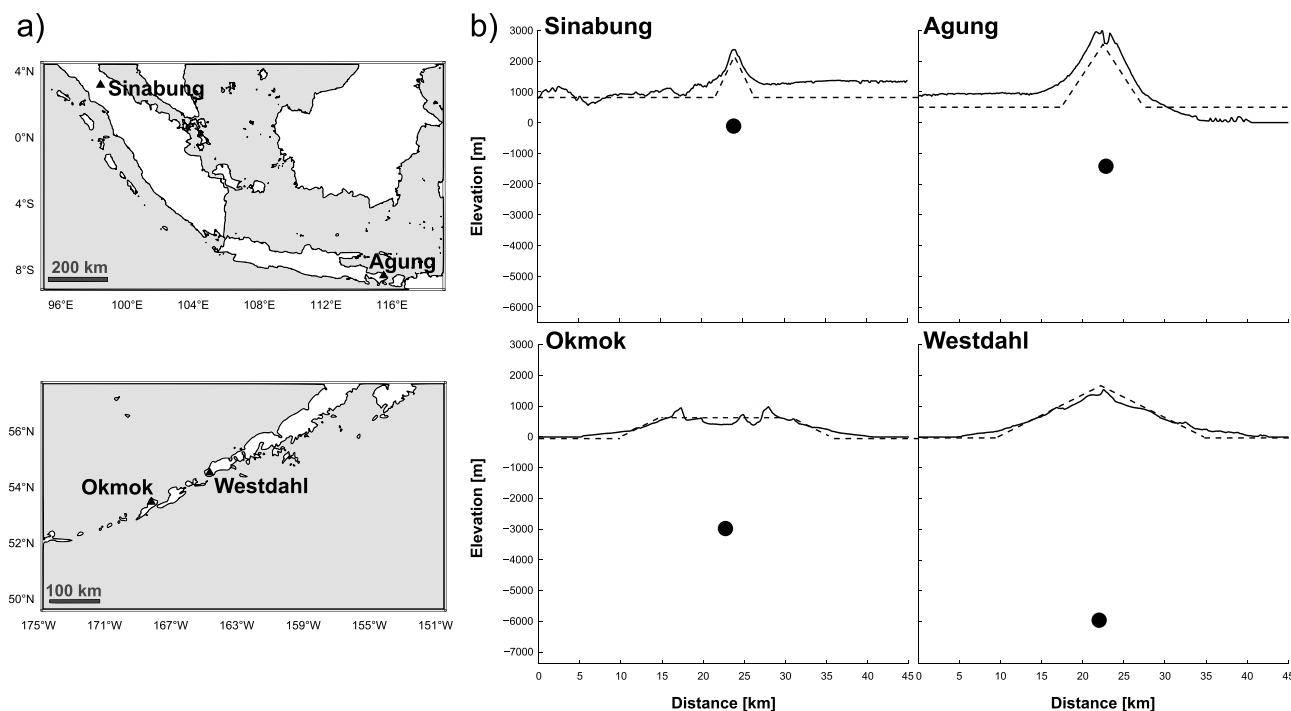


Figure 6. (a) Geographical location of the four volcanoes studied. (b) E-W profiles showing the topography of the edifices (deduced from the SRTM digital elevation model) and the depth of the reservoirs (inferred from InSAR time series). In addition, the surface topography used in our model is shown by dashed lines.

in 1997 and 2008, the caldera floor inflated by almost 1 m, which was modeled by an inflated source with a cumulative change of 0.05 km^3 (Lu & Dzurisin, 2014; Lu et al., 2010).

Westdahl, a basaltic shield (1,654 m) located on Unimak island (Figure 6a, bottom), is one of the largest volcanoes in the Aleutians. Westdahl had only three eruptions since 1900 (Global Volcanism Program, 2013). The last eruption in 1991 produced explosions and lava flows from a 8 km fissure. In January 2004, the Alaska Volcano Observatory detected a strong seismic swarm associated with long-period events beneath the volcano, which could represent a failed eruption (Neal et al., 2005). Westdahl volcano inflated around 20–30 cm between the 1991–1992 eruption and 2010 (Lu et al., 2000, 2003), but no eruption has yet occurred. Both volcanoes show that historical eruptions are associated with lava flows that originate from different fissures. This implies that eruptions at Okmok and Westdahl are not fed by a permanent conduit but rather by successive emplacement of magma intrusions from the reservoir.

4.2. Depth and Volume Change of the Magma Reservoirs

For the four cases, the volume change and the depth of the magma reservoir have already been deduced by the inversion of InSAR time series, using point source model (Mogi, 1958) or pressurized finite sphere embedded in elastic half-space (McTigue, 1987). The Mogi analytical solution for vertical displacements at the surface is defined as $U_z(r) = \frac{(1-\nu)\Delta V|H_c|}{\pi(r^2+H_c^2)^{\frac{3}{2}}}$, where ΔV is the volume change of the source, H_c the center depth of the source, and r the radial distance from the source. In detail, the volume change is a function of the source radius R , the magma overpressure ΔP_m , and the shear modulus of the host rock G through: $\Delta V = \pi R^3 \frac{\Delta P_m}{G}$. This means that to convert displacement to overpressure and vice versa, R and G have to be known. However, geodetic inversions only constrain H_c and ΔV .

At Sinabung and Agung, the ground inflation has been attributed to pressurized spheres at 0.9 and 1.9 km depth below the average elevation of 0.7 and 0.5 km, respectively (Chaussard & Amelung, 2012; Chaussard et al., 2013). The authors also suggested that the volume changes of the Agung and Sinabung reservoir were around 1 km^3 and 0.1 km^3 , respectively. The time series of LOS displacements of these two volcanoes given by Chaussard et al. (2013) are converted into vertical displacements assuming that the magma reservoir axes are located below the summits so that summit displacements are purely vertical (Figures 7a and 7b). The corresponding maximum vertical displacements for Sinabung and Agung are 13 and 16 cm, respectively.

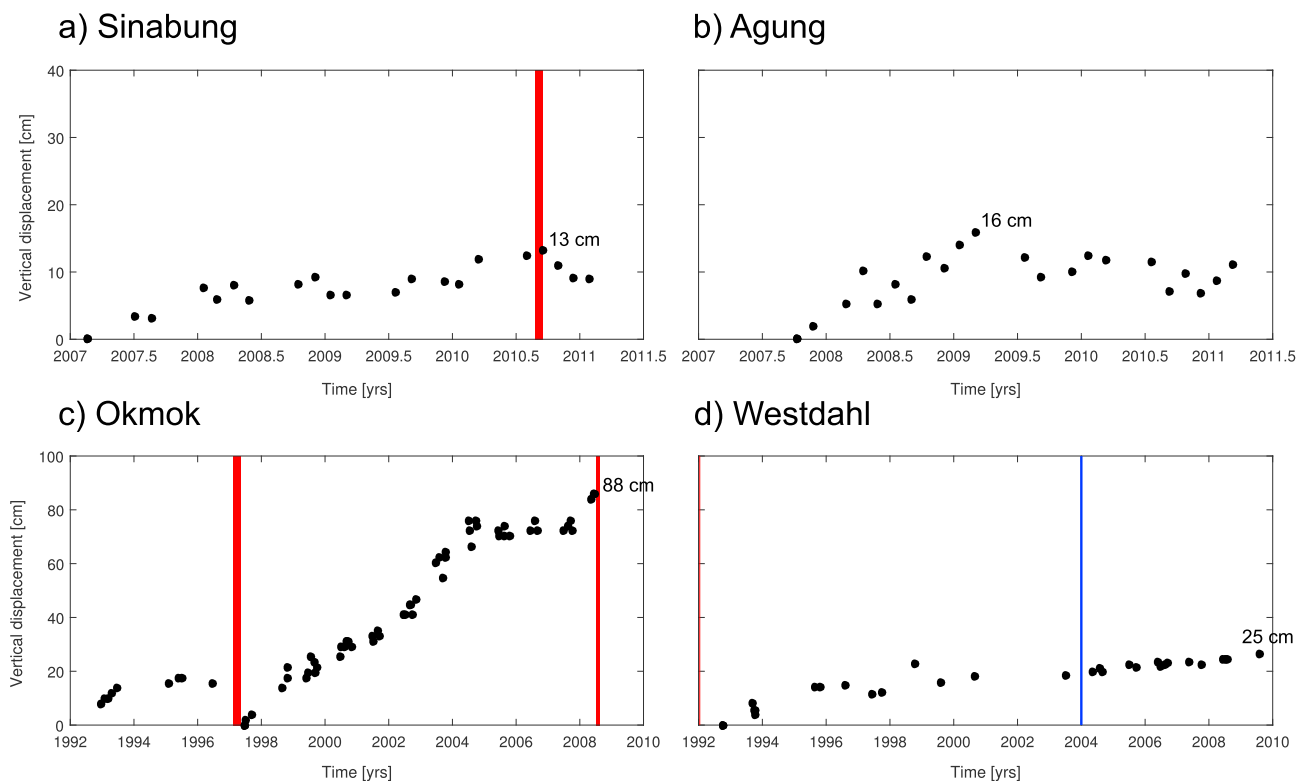


Figure 7. Time series of vertical displacement at Sinabung, Agung (modified from Figures 5 and 7 of Chaussard et al., 2013), Okmok and Westdahl (modified from Figures 6.98 and 6.142 of Lu and Dzurisin, 2014). Red vertical lines underline eruptions and the blue vertical line corresponds to a seismic swarm. On each plot, the maximal displacements inferred from the time series are indicated.

At Sinabung and Agung, as we do not have ground deformation data before the year 2007, these values should therefore be considered as low bounds.

At Okmok, the ground inflation can be explained by a point source at 2.6–3.2 km below sea level (Fournier et al., 2009; Lu et al., 2003; Miyagi et al., 2004). A more realistic Earth model, taking into account the variability of elastic parameters in the crust, gave a source depth of 3.5 km below sea level (Masterlark et al., 2016). At Westdahl, the point source is located deeper at 6 km below sea level (Lu & Dzurisin, 2014). For both Aleutian volcanoes, the inferred cumulative volume change is $50 \cdot 10^6 \text{ m}^3$ (Lu & Dzurisin, 2014). The time series of volume change at Aleutian volcanoes given by Lu and Dzurisin (2014) are converted into vertical displacements at the center of the volcano (Figures 7c and 7d), using the approximation $U_z(r = 0) = \frac{3\Delta V}{4\pi H_c^2}$. The maximal vertical displacements found are 88 cm and 25 cm at Okmok and Westdahl, which, for Okmok, is the total inflation between the 1997 and 2008 eruptions.

As we do not have constraints on the reservoir size, the radius will be considered as a free parameter. The parameters used in the modeling are summarized in Table 2.

Table 2
Model Parameters Used for Studied Cases (See Figure 6b)

Volcano name	Magma reservoir ^a		Volcanic edifice ^b	
	R (m)	H _c (m)	R _e (m)	H _e (m)
Sinabung	100–800	900	2,300	1,250
Agung	100–1,800	1,900	4,700	1,800
Okmok	100–2,000	3,000	12,500	500
Westdahl	100–2,000	6,000	12,500	1,600

^aReservoir depths taken from Chaussard et al. (2013) and Lu and Dzurisin (2014). Values are relative to the base of the volcano, which is assumed to be 0.7 km for Sinabung, 0.5 km for Agung, and 0 km for Okmok and Westdahl. ^bCalculated from the SRTM digital elevation model.

4.3. Morphological Characteristics of the Volcanic Edifices

Elevation profiles show that the volcanic edifices are almost symmetrical, so that they can be approximated by 2-D axisymmetrical models (Figure 6b). The edifices of Sinabung, Agung, and Westdahl are represented as cones defined by its radius and its height. The morphology of Okmok volcano is different than others as the edifice was destroyed by successive collapses. We model it as a cone truncated at 500 m above sea level (Figure 6b). The edifice radius is deduced from the analysis of slope maps and shaded relief images and the edifice height is derived by averaging elevation profiles with different azimuth (Table 2). The average height is measured between the centered summit and the base.

For the Indonesian volcanoes, the base of the edifice is taken as the regional average elevation masking the edifice area, which is respectively 0.7 km for Sinabung and 0.5 km for Agung. For the Aleutian islands, the choice of this base line is more questionable. The reference can be either the sea level or the bottom of the ocean, which strongly depends on which proportion of the volcano is under the sea. Based on the bathymetry map of the Aleutian islands (Zimmermann et al., 2016), volcanic centers are built on top of a 50 km width plateau, located at shallow depth (e.g., 100–500 m below sea level). It means that the basement of Okmok and Westdahl is close to the sea level, and it is therefore more suitable to consider the sea level as reference rather than the bottom of the ocean.

4.4. Shear Modulus Around the Volcanic System

The elastic parameters of the rocks in volcanic environment are poorly constrained. Depending on the volcanic context, authors used in their models different values for the shear modulus, from 2 GPa at Piton de la Fournaise (Reunion island) and Nyamulagira (D. R. of Congo) (Fukushima et al., 2005; Peltier et al., 2008; Wauthier et al., 2013) to 12–30 GPa at Icelandic volcanoes (Pagli et al., 2006; Pinel et al., 2007). Furthermore, the elastic parameters vary vertically and laterally (Auriac et al., 2014; Geyer & Gottsmann, 2008; Long & Grosfils, 2009; Masterlark et al., 2010) and are temperature dependent (e.g., Bakker et al., 2016). Authors pointed out that high temperature may induce inelastic behavior around the magma reservoir associated with low shear modulus (Currenti & Williams, 2014; Currenti et al., 2010; Del Negro et al., 2009; Dragoni & Magnanensi, 1989). According to the values taken, the modeled displacements may change by an order of magnitude. In addition, values for the Poisson's ratio vary with the rock lithology and range from 0.24 to 0.32 for igneous rocks (e.g., Christensen, 1996). However, the influence of the Poisson's ratio in our model results will be much smaller than the effect of the shear modulus and it therefore can be neglected. For each volcano, the Poisson's ratio, ν , is fixed at 0.25 and the shear modulus, G_s , is derived from seismic wave speed measurements:

$$G_s = \frac{(1 - 2\nu)}{2(1 - \nu)} \rho_r V_p^2 \quad (6)$$

with ρ_r the rock density, and V_p the P wave velocity.

At Agung and Sinabung, because there is no local seismic tomography we use results from Toba and Merapi volcanoes. The measured P wave speeds are 3 km.s^{-1} around the Toba magma chamber (Stankiewicz et al., 2010) and 3–4 km.s^{-1} for Merapi (Wagner et al., 2007). Taking a homogeneous rock density of 2,800 kg.m^{-3} , the seismic shear modulus ranges from 8.4 to 14.9 GPa with a mean of 11.6 GPa.

Using seismic tomography at Okmok, Masterlark et al. (2010) found P wave velocities of 2.5 km.s^{-1} in the caldera structure and around the reservoir and 5.7 km.s^{-1} in the surrounding basement. Moreover, they suggested that there is a large contrast of rock density between the caldera ($\rho_r = 1800 \text{ kg.m}^{-3}$) and the basement ($\rho_r = 2800 \text{ kg.m}^{-3}$). The seismic shear moduli G_s calculated from equation (6) are therefore 3.8 GPa below the caldera and 30.3 GPa for the basement.

At Westdahl, the velocity model of McNutt and Jacob (1986) used by the Alaska Volcano Observatory is composed of four layers with velocities of 3.05, 3.44, 5.56, and 6.06 km.s^{-1} for the [3,000 0], [0 –1,790], [–1,790 –3,650], and [–3,650 –6,000] m depth ranges. The corresponding shear moduli are 8.7, 11.0, 28.9, and 34.2 GPa, respectively.

The shear modulus applicable for static mechanical models is lower than the shear modulus for seismic waves because of the presence of fluid-filled pores and cracks (e.g., Gudmundsson, 1990; Wauthier et al., 2012; Zhao et al., 2016). The frequency dependence of the modulus decreases with depth and confining pressure (Ciccotti & Mulargja, 2004). Adelinet et al. (2010) have shown using laboratory measurements of Icelandic basalt that in dry conditions the ratio between the low-frequency and high-frequency bulk moduli is independent of depth and around two thirds. In saturated conditions, the ratio increases from 0.25 at sea level to 1 at a confining pressure of 200 MPa.

For each volcano, we consider models with three different shear moduli, 0.25 G_s , 0.5 G_s , and G_s . For Agung and Sinabung, the models are homogeneous with three shear moduli: 2.9, 5.8, and 11.6 GPa. For Okmok, we use different shear moduli for the caldera and for the surrounding basement. Following the study of Masterlark et al. (2010), the caldera domain is modeled as a semiellipse below the surface with horizontal and vertical axis of 5 km and 2 km, respectively. For the caldera domain, the three values modeled are 0.9, 1.9, and

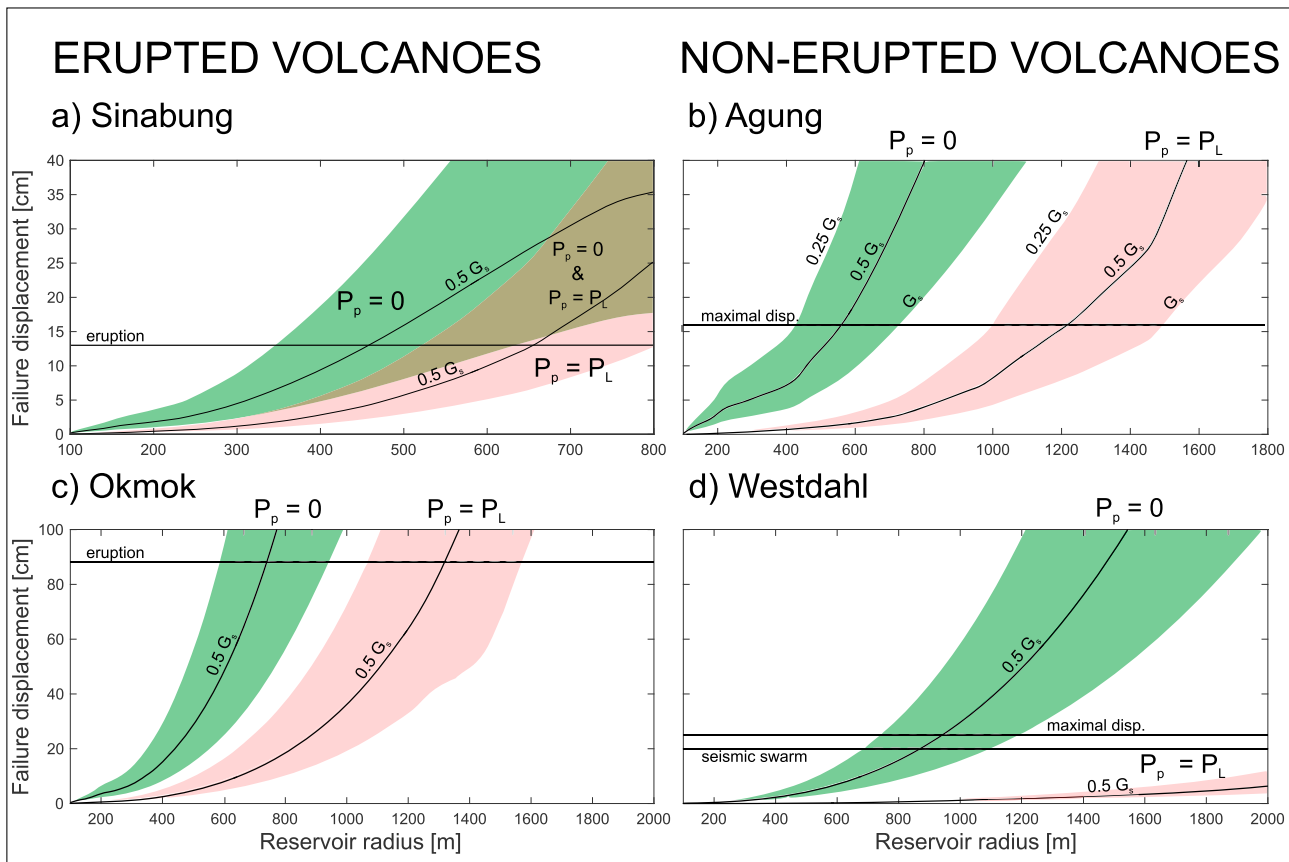


Figure 8. Failure displacements calculated for (a) Sinabung, (b) Agung, (c) Okmok, and (d) Westdahl volcanoes as a function of the reservoir radius and the shear modulus for zero pore fluid pressure (green-shaded area) and lithostatic pore fluid pressure (red-shaded area). The center line of each area corresponds to the displacements associated with $0.5 G_s$. Lower bound and upper bound are respectively for G_s and $0.25G_s$ as shown in Figure 8b. Horizontal lines indicate for each volcano the cumulative displacements obtained from the InSAR time series (Figure 7).

3.8 GPa and for the basement 7.6, 15.15, and 30.3 GPa. For Westdahl, we use the four-layer model from the seismic tomography.

4.5. Observed Displacements Versus Failure Displacements

By applying the failure overpressure ΔP_f at the wall of the magma reservoir, we can calculate the failure displacement U_{Z_f} . This value depends on the shear modulus, the depth, and the size of the reservoir. We use the geodetic reservoir depths and consider the reservoir size as a free parameter. Values for the reservoir radius range from 100 m to 2,000 m for the Aleutian volcanoes. At Sinabung and Agung volcanoes, as their reservoirs are located shallower than 2,000 m (900 and 1,900 m, respectively), the upper bound of the radius will be fixed at 800 and 1,800 m, respectively.

Figure 8 shows, for the four volcanoes, the failure displacement as a function of reservoir radius, shear modulus, and pore fluid pressure conditions. Zero pore fluid pressure is indicated by green shadings and lithostatic pore fluid pressure by red shadings. The figure shows that zero pore fluid conditions produce significantly higher failure displacements than lithostatic pore fluid pressure conditions (independent of reservoir radius and shear modulus). This means that for increasing reservoir radius the failure displacement can be kept constant by increasing the pore fluid pressure (to produce a decrease in overpressure). The figure also shows that a decrease in shear moduli results in an increase of the failure displacements (independent of reservoir radius and the pore fluid pressure conditions).

We are aware that the reservoir depth given for each volcano is known with some uncertainty, which may also influence the failure displacements calculated. Under zero pore pressure, the overpressure increases with the reservoir depth. As a consequence, a variation of 20% of the reservoir depth does not have significant effect on the failure displacements (Figure S1 in the supporting information). On the contrary, under lithostatic pore

pressure, the variations of the failure overpressure with depth are small; therefore, the failure displacement largely decreases with the increase of the reservoir depth. In this case, an increase of 20% of the depth would have the same effect than an increase of the shear modulus by a factor of 2 (Figure S1, supporting information). Uncertainties of failure displacements due to reservoir depth are therefore very similar to the uncertainties already deduced from the shear modulus (Figure 8).

At Sinabung, the observed displacement of 13 cm (prior to the 2010 eruption) is reached under zero pore fluid pressure conditions for reservoirs with 350–640 m radius and under lithostatic pore fluid pressure conditions for reservoirs with 520–800 m radius. The same failure displacement can be produced by a range of pore fluid pressure conditions. This shows that the interpretation of the observed inflation in terms of the fluid pressure conditions (assuming that there was no inflation prior to 2007, i.e., that it equals the failure displacement) would require information on the reservoir radius and the shear modulus.

Agung inflated by 16 cm but there was no eruption, which suggests that inflation remained below the failure displacement. Using Figure 8b we obtain a lower bound of the reservoir radius. Assuming a shear modulus of $0.5 G_s$, we find that Agung's reservoir radius must be larger than 560 and 1,220 m for zero and lithostatic pore fluid pressure conditions, respectively.

Okmok inflated by 88 cm between the 1997 and 2008 eruptions. The models show that under zero pore fluid pressure conditions such failure displacement can be reached for reservoirs with radii between 600 and 950 m and under lithostatic pore fluid pressure conditions for radii between 1,050 and 1,550 m. Fournier (2008) used GPS data and thermodynamic models to constrain the radius of the reservoir to be between 1 and 2 km. Combined with our modeling results, this would suggest lithostatic pore fluid pressure conditions for this volcano.

Westdahl has inflated by 25 cm since the 1991–1992 eruption without any new eruption at the surface. As for Agung, this observation may suggest a combination of pore fluid pressure conditions and reservoir radius so that the failure displacement is above this value. Using Figure 8d, we find that the pore fluid pressure conditions should be lower than lithostatic and the reservoir radius must be larger than 700 m. However, the caveat for this interpretation is a seismic swarm in January 2004 (Neal et al., 2005), which could indicate that the system had reached a stress state sufficient to break rock after only 20 cm of inflation. The swarm could represent a failed eruption (tensile failure of the reservoir wall without propagation of the intrusion to the surface). From Figure 8d, we find that for $P_p = 0$ and $G = 0.5 G_s$, an 850 m radius reservoir can produce the observed failure displacement of 20 cm. For lithostatic pore fluid pressure conditions, the failure displacements modeled are always less than 20 cm, which cannot explain the failed eruption.

To summarize, for shallow reservoirs (less than 1 km), such as Sinabung, it is impossible to discriminate between the two pore fluid pressure assumptions as failure overpressures are similar. However, for deeper magma reservoirs, the difference between failure displacements becomes significant. At Agung, the absence of eruption indicates that the radius of the reservoir must be larger than 560 m. At Okmok, the 2008 eruption seems to be associated with high pore fluid pressure conditions whereas the failed eruption at Westdahl would suggest pore pressure conditions much lower than lithostatic.

5. Discussion

5.1. Influence of Magma Reservoir, Volcanic Edifice, and Pore Fluid Pressure on Failure Conditions

Table 3 summarizes the main results of the parametric study (section 3) on the failure overpressure. An initial model without edifice with a magma chamber with $R = 1,000$ m at $H_t = -2,000$ m is given as a reference. As the depth of the reservoir decreases, the failure overpressure decreases, which promotes the initiation of magma intrusions. The effect is nearly negligible for lithostatic pore fluid pressure (a few megapascals), but is significant for zero pore fluid pressure as a 1 km reduction in reservoir depth leads to a decrease of the failure overpressure by 60 MPa.

The load of the volcanic edifice also affects the failure conditions. A 1,250 m high edifice with 5,000 m radius reduces the failure overpressure by about 15 MPa from the reference model for both pore fluid pressure conditions. Later, when the edifice widens, the failure overpressure increases (by 5 MPa for an 8,000 m radius). When the edifice collapses and/or a caldera forms, the load of the edifice is suppressed and the failure overpressure is similar to the reference model. The effect of stress perturbations, such as the construction/destruction of an

Table 3

Summary of How Failure Overpressures of a Spherical Magma Reservoir Vary With Reservoir Depth, Edifice Loading, and Pore Fluid Pressure

Model configuration	Variables (m)	Failure overpressure (MPa)	N° figure
		$P_p = P_L$	$P_p = 0$
Reference model	$R = 1,000 \quad H_t = -2,000$	19	132
Reservoir depth decrease	$R = 1,000 \quad H_t = -1,000$	17	71 ^a
Edifice loading			
Small edifice	$R_e = 3,000 \quad H_e = 1,250$	5 ^a	116
Large edifice	$R_e = 8,000 \quad H_e = 1,250$	11	122
Caldera	$R_e = 8,000 \quad H_e = 500$	17	128

Note. The initial model is without topography and given as a reference. In the loading models, the size and the depth of the reservoir are the same as the initial model.

^aThis indicates the minimum value for each pore fluid pressure conditions.

edifice on failure overpressure, is independent of the value of the pore fluid pressure. It means that the studies focusing on the influence of external stress changes on reservoir failure do not need to take into account the pore fluid pressure conditions.

For lithostatic pore fluid pressure, the failure overpressure is more sensitive to edifice loading than to reservoir depth. Indeed, the minimum failure overpressure is associated with the small edifice case (superscript "a" in Table 3). In contrast, for zero pore fluid pressure, the failure overpressure is more sensitive to reservoir depth than to edifice loading. The minimum failure overpressure is found for a reservoir depth of 1 km (superscript "a" in Table 3).

Although both reservoir depth and edifice loading have an effect on the failure overpressure, the strongest effect is the pore fluid pressure itself. For the reference model, the failure overpressure decreases from 132 to 19 MPa for a pore fluid pressure increases from 0 to P_L . The effect would even be larger for deeper magma reservoirs. Our study underlines that the effect of the pore fluid pressure on the failure overpressure of spherical reservoirs is an order of magnitude larger than stress perturbations due to loading. The estimation of the overpressure to initiate an intrusion therefore requires knowledge about the pore fluid pressure conditions and the reservoir depth.

5.2. Model Assumptions and Limitations

In our study, we have neglected the anelastic effects associated with viscoelastic rheology, which describes the response of large and long-lived silicic magmatic systems (de Silva & Gregg, 2014; Gregg et al., 2012; Jellinek & DePaolo, 2003; Simakin & Ghassemi, 2010). Studies have been conducted for Campi Flegrei (Bonafede et al., 1986; Dragoni & Magnanensi, 1989) and Long Valley (Newman et al., 2001, 2006). Viscoelasticity affects both ground deformation and the conditions for failure of the reservoir. A pressurized magma reservoir embedded in a viscoelastic medium will be associated with more surface displacement than one embedded in an elastic medium due to the viscous relaxation of the rocks. Following eruptions, viscoelasticity may lead to deflation, even if the magma chamber is replenished (Segall, 2016). In addition, heated rocks become ductile and can support larger stress without fracturing (Gregg et al., 2012; Jellinek & DePaolo, 2003). Gregg et al. (2012) demonstrate that viscoelasticity has little effect on the failure overpressure for small reservoirs with volume less than a hundred cubic kilometer (which corresponds to a radius of almost 3 km). The reservoirs of Okmok, Sinabung, and Agung are located at depths shallower than 3 km. Westdahl has a deeper source (6 km), but there is no evidence for a large magma reservoir. It is unlikely that the reservoir volumes of the four volcanoes studied are larger than 100 km³, strongly suggesting that the elastic assumption is valid. In such assumption, the conditions of failure discussed in our study do not depend on the rate of ground deformation.

We have also neglected the effect of pore fluid pressure on ground deformation estimation. In our modeling, host rock medium behaves elastically as pore pressure effect is only considered at the vicinity of the reservoir. This assumption is valid if we consider that the accumulation of fluid is localized around magma reservoirs. In this case, the poroelastic medium will only be a ring around the magma reservoir.

Previous studies have already shown that ellipticity of the reservoir influences the failure conditions both in location (Grosfils, 2007) and amplitude (Albino et al., 2010). For example, for oblate ellipsoid, the failure overpressure is smaller compared to spherical reservoir, because tensile stress concentrates at the extremity of the horizontal axis, where the curvature is highest. As a consequence, the failure displacement would also be smaller. Only at Okmok, Lu et al. (2010) found from the inversion of InSAR data an ellipticity ratio of 1.04, which nearly corresponds to a sphere.

Our failure models provide the overpressure for the failure of a magma reservoir. However, reservoir failure does not necessarily produce an eruption, as new intrusions can be stalled at depth due to a decrease in magma supply, magma freezing due to slow ascent, viscosity increases by magma degassing, and heat loss or density barriers in the crust (Gudmundsson, 2002; Moran et al., 2011; Taisne et al., 2011). As mentioned above, the 2004 Westdahl seismic swarm could represent a failed eruption for which the overpressure was not sufficient to propagate the intrusions to the surface. Magma propagation is a complex problem (see Rivalta et al. (2015) for a review) and is not yet considered in our models.

5.3. Pore Fluid Pressure Conditions Around Magma Reservoirs

Experimental rock mechanics predict that the brittle frictional strength linearly increases with depth in the upper crust (Brace & Kohlstedt, 1980). Such linear relationship is based on the assumption of hydrostatic pore fluid pressure and implies that the crust is close to a critical state of failure. This is in good accordance with stress data from deep boreholes such as the KTB borehole in Germany (e.g., Townend & Zoback, 2000; Zoback, 2010). The pore fluid pressure is usually considered to be in a hydrostatic equilibrium equal to the weight of a column of water, $P_H = \rho_H g z$ with ρ_H the density of water. Zoback and Townend (2001) suggested that hydrostatic pore fluid pressure could be sustained to a depth of as much as 12 km. However, in particular contexts, the pore fluid pressure can be in excess of hydrostatic (e.g., Moos & Zoback, 1993). Suprahydrostatic pore fluid pressure can be due to an undercompaction during rapid burial of sediments, lateral compression, release of water from minerals, or expansion of the fluid volume (Hantschel & Kauerauf, 2009). Evidence for suprahydrostatic pore fluid pressure was also found around magmatic intrusions, mud volcanoes, hydrothermal vents, or faults, showing that pore fluid pressure is spatially heterogeneous (Jamtveit et al., 2004). Under undrained conditions, the pore fluid pressure can be between hydrostatic and lithostatic. Under drained conditions with the fluids escaping from the pores, the pore fluid pressure can be lower than hydrostatic.

There is little information about the pore fluid pressure surrounding magma reservoirs. If fluids originate from the magma, the pore fluid pressure in the adjacent rock would be similar to the magma pressure. Over a narrow zone of a few meters to tens of meters the fluid pressure decreases with a steep gradient to hydrostatic or subhydrostatic, depending on depth and the confining pressure and whether a hydrothermal system exists. Ductile flow near the brittle-plastic transition could act to reduce the permeability of the silicic rock, potentially providing a self-sealing mechanism (Fournier, 2007). For Long Valley Caldera, the variability of the stress directions constrained by both borehole breakouts and earthquake focal mechanisms suggest near-lithostatic pore fluid pressure conditions (Moos & Zoback, 1993).

Therefore, the two approaches for the failure of magma reservoirs described in section 2.1 are both correct, but correspond to different drainage conditions (Gerbault, 2012; Gerbault et al., 2012; Grosfils et al., 2015). The failure models discussed by Gudmundsson (2002), Pinel and Jaupart (2005), and Tait et al. (1989) considered the host rock as an undrained medium with lithostatic pore fluid pressure. Grosfils (2007) considers a drained medium with zero pore fluid pressure where all the fluids have escaped from the rock pores. These two approaches are end-members for the range of possible pore fluid pressure conditions.

At Okmok caldera, the intereruption displacement together with independent information about the size of the magma reservoir suggests near-lithostatic pore fluid pressure, whereas the inflation at Westdahl without eruption at the surface suggests pore fluid pressures significantly lower than lithostatic. Knowing the failure pressure, we can derive the critical volume change required before an eruption. Considering lithostatic pore pressure, the total volume change at Okmok before an eruption is $13.5 \times 10^6 \text{ m}^3$. Under zero pore pressure, the total volume change at Westdahl before an eruption is $52.3 \times 10^6 \text{ m}^3$. Due to the difference of pore pressure conditions, the failure of Westdahl's reservoir requires a volume change 4 times larger than the one required for the failure of Okmok's reservoir. Under the assumption that both shallow reservoirs are supplied at the same magma supply rate from a deeper source, it means that the frequency of failure should be 4 times higher at Okmok in comparison with Westdahl. This is in accordance with the eruption records that reported 11 confirmed eruptions at Okmok and 3 eruptions at Westdahl between 1900 and 2017. Pore pressure difference can

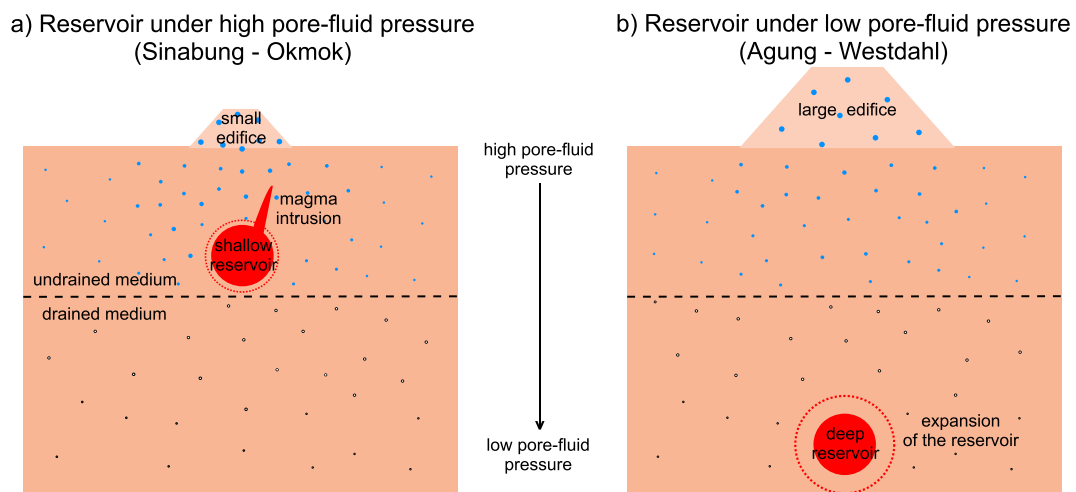


Figure 9. Sketch explaining the difference of eruptive behavior based on the pore fluid pressure conditions of the host rock: (a) a shallow magma reservoir embedded in a high pore fluid pressure host rock promotes the initiation of a magma intrusion, which may lead to an eruption; (b) a deep magma reservoir within a low pore fluid pressure host rock favors the expansion of the reservoir rather than the initiation of an intrusion.

therefore be an explanation for the difference of eruption frequency between these two Aleutian volcanoes. The development of high pore pressure at Okmok promotes the failure of the reservoir and the occurrence of frequent intrusions of small volume (Figure 9a). Under low pore fluid pressure conditions such as at Westdahl, the failure of the reservoir requires a large volume change, which could explain the low frequency of eruptions (Figure 9b).

The importance of pore fluid pressure changes for earthquake generation is well established (Bell & Nur, 1978; Parotidis et al., 2003; Shapiro et al., 2003; Talwani & Acree, 1984; Zoback & Gorelick, 2012). An increase of pore fluid pressure in the crust reduces the normal stress on faults, which favors Coulomb shear failure. It has been shown that the increase of pore fluid pressure produced by heavy rainfall events (monsoons, typhoons, or hurricanes) can trigger earthquakes (see Costain & Bollinger, 2010; Hainzl et al., 2006). Our study shows that the pore fluid pressure also affects the mode of transport of the magma by playing a role in the failure of magma reservoirs. In theory, a pore fluid pressure increase could trigger an eruption without any increase of the reservoir pressure, which may be an explanation why some eruptions occur without significant preeruptive inflation.

6. Conclusions

1. We show that the two commonly used approaches to investigate the failure of magma reservoirs (Gudmundsson, 2012; Grosfils et al., 2015) are end-members in a framework that accounts for the pore fluid pressure conditions in the host rock. The pore fluid pressure around the reservoir has a strong influence on the magma overpressure required for tensile failure of the reservoir wall. It is stronger than the influence of the depth of the reservoir or the loading stress of the volcanic edifice.
2. Whereas the failure overpressure is dependent on the pore fluid pressure conditions, the changes of the failure overpressure due to stress perturbations (e.g., growth of an edifice, caldera formation) are independent of the pore fluid pressure conditions.
3. The ground surface inflation due to reservoir pressurization depends on the reservoir location, geometry, and elastic properties of the rock. The interpretation of geodetically detected inflation in terms of eruption potential thus requires knowledge about (i) the pore fluid pressure conditions in the vicinity of a magma reservoir, (ii) the reservoir depth, (iii) the reservoir radius, and (iv) the shear modulus of the surrounding host rock.
4. From the four volcanoes studied, the inferred pore fluid pressure conditions are likely supraphydrostatic for the two erupted volcanoes (Sinabung and Okmok) and subhydrostatic for the nonerupted volcanoes (Agung and Westdahl). High pore fluid pressure conditions favor the initiation of intrusions, whereas low pore fluid pressure conditions make the initiation of intrusions difficult and favor the growth of reservoirs.

Acknowledgments

We thank the National Aeronautics and Space Administration (NASA) for support (grant NNX14AQ01G). All the InSAR time series used in our paper are derived from previous works and cited in the references. We would like to also thank E. Grosfils, A. Geyer, M. Nikkhoo and an anonymous reviewer for their insightful comments on the paper.

References

- Acocella, V., Di Lorenzo, R., Newhall, C., & Scandone, R. (2015). An overview of recent (1988 to 2014) caldera unrest: Knowledge and perspectives. *Reviews of Geophysics*, 53, 896–955. <https://doi.org/10.1002/2015RG000492>
- Acocella, V., & Funiciello, F. (2010). Kinematic setting and structural control of arc volcanism. *Earth and Planetary Science Letters*, 289(1), 43–53.
- Adelinet, M., Fortin, J., Guéguen, Y., Schubnel, A., & Geoffroy, L. (2010). Frequency and fluid effects on elastic properties of basalt: Experimental investigations. *Geophysical Research Letters*, 37, L02303. <https://doi.org/10.1029/2009GL041660>
- Albino, F., Pinel, V., & Sigmundsson, F. (2010). Influence of surface load variations on eruption likelihood: Application to two Icelandic subglacial volcanoes, Grímsvötn and Katla. *Geophysical Journal International*, 181(3), 1510–1524. <https://doi.org/10.1111/j.1365-246X.2010.04603.x>
- Amoruso, A., Crescentini, L., Linde, A. T., Sacks, I. S., Scarpa, R., & Romano, P. (2007). A horizontal crack in a layered structure satisfies deformation for the 2004–2006 uplift of Campi Flegrei. *Geophysical Research Letters*, 34, L22313. <https://doi.org/10.1029/2007GL031644>
- Auriac, A., Sigmundsson, F., Hooper, A., Spaans, K. H., Björnsson, H., Palsson, F., ... Feigl, K. L. (2014). InSAR observations and models of crustal deformation due to a glacial surge in Iceland. *Geophysical Journal International*, 198(3), 1329–1341.
- Bagnardi, M., & Amelung, F. (2012). Space-geodetic evidence for multiple magma reservoirs and subvolcanic lateral intrusions at Fernandina Volcano, Galápagos Islands. *Journal of Geophysical Research*, 117, B10406. <https://doi.org/10.1029/2012JB009465>
- Bakker, R. R., Frehner, M., & Lupi, M. (2016). How temperature-dependent elasticity alters host rock/magmatic reservoir models: A case study on the effects of ice-cap unloading on shallow volcanic systems. *Earth and Planetary Science Letters*, 456, 16–25.
- Beauducel, F., De Natale, G., Obrizzo, F., & Pingue, F. (2004). 3-D modelling of Campi Flegrei ground deformations: Role of caldera boundary discontinuities. In *Geodetic and Geophysical Effects Associated with Seismic and Volcanic Hazards* (pp. 1329–1344). Basel, Switzerland: Springer.
- Bell, M. L., & Nur, A. (1978). Strength changes due to reservoir-induced pore pressure and stresses and application to Lake Oroville. *Journal of Geophysical Research*, 83(B9), 4469–4483.
- Biggs, J., Ebmeier, S. K., Aspinall, W. P., Lu, Z., Pritchard, M. E., Sparks, R. S. J., & Mather, T. A. (2014). Global link between deformation and volcanic eruption quantified by satellite imagery. *Nature Communications*, 5, 3471.
- Björnsson, A., Johnsen, G., Sigurdsson, S., Thorbergsson, G., & Tryggvason, E. (1979). Rifting of the plate boundary in North Iceland 1975–1978. *Journal of Geophysical Research*, 84(B6), 3029–3038.
- Bonafede, M., Dragoni, M., & Quarenì, F. (1986). Displacement and stress fields produced by a centre of dilation and by a pressure source in a viscoelastic half-space: Application to the study of ground deformation and seismic activity at Campi Flegrei, Italy. *Geophysical Journal International*, 87(2), 455–485.
- Brace, W. F., & Kohlstedt, D. L. (1980). Limits on lithospheric stress imposed by laboratory experiments. *Journal of Geophysical Research*, 85(B11), 6248–6252.
- Burt, M. L., Wedge, G., & Scott, W. A. (1994). Simple stochastic modelling of the eruption history of a basaltic volcano: Nyamuragira, Zaire. *Bulletin of Volcanology*, 56(2), 87–97.
- Byers, F. M. (1959). Geology of Umnak and Bogoslof Islands, Aleutian Islands, Alaska (Tech. Rep.). United States Government Office.
- Cervelli, P. F., Fournier, T., Freymueller, J., & Power, J. A. (2006). Ground deformation associated with the precursory unrest and early phases of the January 2006 eruption of Augustine Volcano, Alaska. *Geophysical Research Letters*, 33, L18304. <https://doi.org/10.1029/2006GL027219>
- Chang, W.-L., Smith, R. B., Wicks, C., Farrell, J. M., & Puskas, C. M. (2007). Accelerated uplift and magmatic intrusion of the Yellowstone caldera, 2004 to 2006. *Science*, 318(5852), 952–956.
- Chaussard, E., & Amelung, F. (2012). Precursory inflation of shallow magma reservoirs at west Sunda volcanoes detected by InSAR. *Geophysical Research Letters*, 39, L21311. <https://doi.org/10.1029/2012GL053817>
- Chaussard, E., & Amelung, F. (2014). Regional controls on magma ascent and storage in volcanic arcs. *Geochemistry, Geophysics, Geosystems*, 15, 1407–1418. <https://doi.org/10.1002/2013GC005216>
- Chaussard, E., Amelung, F., & Aoki, Y. (2013). Characterization of open and closed volcanic systems in Indonesia and Mexico using InSAR time series. *Journal of Geophysical Research: Solid Earth*, 118, 3957–3969. <https://doi.org/10.1002/jgrb.50288>
- Chestler, S. R., & Grosfils, E. B. (2013). Using numerical modeling to explore the origin of intrusion patterns on Fernandina volcano, Galapagos Islands, Ecuador. *Geophysical Research Letters*, 40, 4565–4569. <https://doi.org/10.1002/grl.50833>
- Christensen, N. I. (1996). Poisson's ratio and crustal seismology. *Journal of Geophysical Research*, B2, 3139–3156.
- Ciccotti, M., & Mularia, F. (2004). Differences between static and dynamic elastic moduli of a typical seismogenic rock. *Geophysical Journal International*, 157(1), 474–477.
- Costain, J. K., & Bollinger, G. A. (2010). Review: Research results in hydroseismicity from 1987 to 2009. *Bulletin of the Seismological Society of America*, 100(5A), 1841–1858.
- Currenti, G., Bonaccorso, A., Del Negro, C., Scandura, D., & Boschi, E. (2010). Elasto-plastic modeling of volcano ground deformation. *Earth and Planetary Science Letters*, 296(3), 311–318.
- Currenti, G., & Williams, C. A. (2014). Numerical modeling of deformation and stress fields around a magma chamber: Constraints on failure conditions and rheology. *Physics of the Earth and Planetary Interiors*, 226, 14–27. <https://doi.org/10.1016/j.pepi.2013.11.003>
- De Natale, G., Petruzzoli, S. M., & Pingue, F. (1997). The effect of collapse structures on ground deformations in calderas. *Geophysical Research Letters*, 24(13), 1555–1558.
- de Silva, S. L., & Gregg, P. M. (2014). Thermomechanical feedbacks in magmatic systems: Implications for growth, longevity, and evolution of large caldera-forming magma reservoirs and their supereruptions. *Journal of Volcanology and Geothermal Research*, 282, 77–91.
- Del Negro, C., Currenti, G., & Scandura, D. (2009). Temperature-dependent viscoelastic modeling of ground deformation: Application to Etna volcano during the 1993–1997 inflation period. *Physics of the Earth and Planetary Interiors*, 172(3), 299–309.
- Di Vito, M. A., Isaia, R., Orsi, G., Southon, J., De Vita, S., d'Antonio, M., ... Piochi, M. (1999). Volcanism and deformation since 12,000 years at the Campi Flegrei caldera (Italy). *Journal of Volcanology and Geothermal Research*, 91(2), 221–246.
- Dragon, M., & Magnanensi, C. (1989). Displacement and stress produced by a pressurized, spherical magma chamber, surrounded by a viscoelastic shell. *Physics of the Earth and Planetary Interiors*, 56(3), 316–328.
- Dvorak, J. J., & Dzurisin, D. (1993). Variations in magma supply rate at Kilauea volcano, Hawaii. *Journal of Geophysical Research*, 98(B12), 22,255–22,268.
- Dzurisin, D. (2003). A comprehensive approach to monitoring volcano deformation as a window on the eruption cycle. *Reviews of Geophysics*, 41(1), 1001. <https://doi.org/10.1029/2001RG000107>
- Ewart, J. A., Voight, B., & Björnsson, A. (1991). Elastic deformation models of Krafla Volcano, Iceland, for the decade 1975 through 1985. *Bulletin of Volcanology*, 53(6), 436–459.

- Farquharson, J., Heap, M. J., Baud, P., Reuschlé, T., & Varley, N. R. (2016). Pore pressure embrittlement in a volcanic edifice. *Bulletin of Volcanology*, 78(1), 6.
- Feigl, K. L., Le Mevel, H., Tabrez Ali, S., Cordova, L., Andersen, N. L., DeMets, C., & Singer, B. S. (2014). Rapid uplift in Laguna del Maule volcanic field of the Andean Southern Volcanic zone (Chile) 2007–2012. *Geophysical Journal International*, 196(2), 885–901. <https://doi.org/10.1093/gji/ggt438>
- Fournier, R. O. (2007). Hydrothermal systems and volcano geochemistry. In D. Dzurisin (Ed.), *Volcano Deformation: Geodetic Monitoring Techniques* (pp. 323–341). Berlin: Springer.
- Fournier, T., Freymueller, J., & Cervelli, P. (2009). Tracking magma volume recovery at Okmok volcano using GPS and an unscented Kalman filter. *Journal of Geophysical Research*, 114, B02405. <https://doi.org/10.1029/2008JB005837>
- Fournier, T. J. (2008). Analysis and interpretation of volcano deformation in Alaska: Studies from Okmok and Mt. Veniaminof volcanoes (PhD thesis). University of Alaska Fairbanks.
- Fukushima, Y., Cayol, V., & Durand, P. (2005). Finding realistic dike models from interferometric synthetic aperture radar data: The February 2000 eruption at Piton de la Fournaise. *Journal of Geophysical Research*, 110, B03206. <https://doi.org/10.1029/2004JB003268>
- Geist, D. J., Harpp, K. S., Naumann, T. R., Poland, M., Chadwick, W. W., Hall, M., & Rader, E. (2008). The 2005 eruption of Sierra Negra volcano, Galápagos, Ecuador. *Bulletin of Volcanology*, 70(6), 655–673.
- Gerbault, M. (2012). Pressure conditions for shear and tensile failure around a circular magma chamber; insight from elasto-plastic modelling. *Geological Society, London, Special Publications*, 367(1), 111–130.
- Gerbault, M., Cappa, F., & Hassani, R. (2012). Elasto-plastic and hydromechanical models of failure around an infinitely long magma chamber. *Geochemistry, Geophysics, Geosystems*, 13, Q03009. <https://doi.org/10.1029/2011GC003917>
- Geyer, A., & Bindeman, I. (2011). Glacial influence on caldera-forming eruptions. *Journal of Volcanology and Geothermal Research*, 202(1–2), 127–142. <https://doi.org/10.1016/j.jvolgeores.2011.02.001>
- Geyer, A., & Gottsmann, J. (2008). Ground deformation at collapse calderas: Influence of host rock lithology and reservoir multiplicity. In *Earth and Environmental Science, IOP Conference Series* (Vol. 3, pp. 012017). IOP.
- Geyer, A., & Gottsmann, J. (2010). The influence of mechanical stiffness on caldera deformation and implications for the 1971–1984 Rabaul uplift (Papua New Guinea). *Tectonophysics*, 483(3), 399–412.
- Geyer, A., & Martí, J. (2009). Stress fields controlling the formation of nested and overlapping calderas: Implications for the understanding of caldera unrest. *Journal of Volcanology and Geothermal Research*, 181(3), 185–195.
- Global Volcanism Program (2013). *Volcanoes of the World* (v. 4.6.1). In E. Venzke (Ed.). Smithsonian Institution. <https://doi.org/10.5479/si.GVP.VOTW4-2013>
- Gottsmann, J., Rymer, H., & Berrino, G. (2006). Unrest at the Campi Flegrei caldera (Italy): A critical evaluation of source parameters from geodetic data inversion. *Journal of Volcanology and Geothermal Research*, 150(1), 132–145.
- Gregg, P., de Silva, S., Grosfils, E., & Parmigiani, J. (2012). Catastrophic caldera-forming eruptions: Thermomechanics and implications for eruption triggering and maximum caldera dimensions on Earth. *Journal of Volcanology and Geothermal Research*, 241–242, 1–12. <https://doi.org/10.1016/j.jvolgeores.2012.06.009>
- Gressier, J.-B., Mourguet, R., Bodet, L., Matthieu, J.-Y., Galland, O., & Cobbold, P. (2010). Control of pore fluid pressure on depth of emplacement of magmatic sills: An experimental approach. *Tectonophysics*, 489(1), 1–13.
- Grosfils, E. B. (2007). Magma reservoir failure on the terrestrial planets: Assessing the importance of gravitational loading in simple elastic models. *Journal of Volcanology and Geothermal Research*, 166(2), 47–75. <https://doi.org/10.1016/j.jvolgeores.2007.06.007>
- Grosfils, E. B., McGovern, P. J., Gregg, P. M., Galgana, G. A., Hurwitz, D. M., Long, S. M., & Chestler, S. R. (2015). Elastic models of magma reservoir mechanics: A key tool for investigating planetary volcanism. *Geological Society, London, Special Publications*, 401(1), 239–267. <https://doi.org/10.1144/SP401.2>
- Gudmundsson, A. (1988). Effect of tensile stress concentration around magma chambers on intrusion and extrusion frequencies. *Journal of Volcanology and Geothermal Research*, 35(3), 179–194.
- Gudmundsson, A. (1990). Emplacement of dikes, sills and crustal magma chambers at divergent plate boundaries. *Tectonophysics*, 176(3–4), 257–275.
- Gudmundsson, A. (2002). Emplacement and arrest of sheets and dykes in central volcanoes. *Journal of Volcanology and Geothermal Research*, 116(3), 279–298.
- Gudmundsson, A. (2006). How local stresses control magma-chamber ruptures, dyke injections, and eruptions in composite volcanoes. *Earth-Science Reviews*, 79(1–2), 1–31. <https://doi.org/10.1016/j.earscirev.2006.06.006>
- Gudmundsson, A. (2012). Strengths and strain energies of volcanic edifices: Implications for eruptions, collapse calderas, and landslides. *Natural Hazards and Earth System Science*, 12(7), 2241–2258.
- Gudmundsson, A., & Brenner, S. L. (2001). How hydrofractures become arrested. *Terra Nova*, 13(6), 456–462.
- Haimson, B. C., & Rummel, F. (1982). Hydrofracturing stress measurements in the Iceland research drilling project drill hole at Reydarfjordur, Iceland. *Journal of Geophysical Research*, 87(B8), 6631–6649.
- Hainzl, S., Kraft, T., Wassermann, J., Igel, H., & Schmedes, E. (2006). Evidence for rainfall-triggered earthquake activity. *Geophysical Research Letters*, 33, L19303. <https://doi.org/10.1029/2006GL027642>
- Hantschel, T., & Kauerauf, A. I. (2009). Pore pressure, compaction and tectonics. In *Fundamentals of basin and petroleum systems modeling* (pp. 31–101). Berlin: Springer.
- Hill, D. P. (1984). Monitoring unrest in a large silicic caldera, the Long Valley-Inyo craters volcanic complex in east-central California. *Bulletin of Volcanology*, 47(2), 371–395.
- Hughes, G. R., & Mahood, G. A. (2011). Silicic calderas in arc settings: Characteristics, distribution, and tectonic controls. *Geological Society of America Bulletin*, 123(7–8), 1577–1595.
- Hurwitz, D. M., Long, S. M., & Grosfils, E. B. (2009). The characteristics of magma reservoir failure beneath a volcanic edifice. *Journal of Volcanology and Geothermal Research*, 188(4), 379–394. <https://doi.org/10.1016/j.jvolgeores.2009.10.004>
- Hurwitz, S., & Johnston, M. J. (2003). Groundwater level changes in a deep well in response to a magma intrusion event on Kilauea Volcano, Hawai'i. *Geophysical Research Letters*, 30(22), 2173. <https://doi.org/10.1029/2003GL018676>
- Jaeger, C. (1979). *Rock mechanics and engineering*. Cambridge, UK: Cambridge University Press.
- Jamtveit, B., Svensen, H., Podladchikov, Y. Y., & Planke, S. (2004). Hydrothermal vent complexes associated with sill intrusions in sedimentary basins. *Physical Geology of High-Level Magmatic Systems*, 234, 233–241.
- Jeffery, G. B. (1921). Plane stress and plane strain in bipolar co-ordinates. *Philosophical Transactions of the Royal Society of London. Series A, Containing Papers of a Mathematical or Physical Character*, 221, 265–293.
- Jellinek, A. M., & DePaolo, D. J. (2003). A model for the origin of large silicic magma chambers: Precursors of caldera-forming eruptions. *Bulletin of Volcanology*, 65(5), 363–381. <https://doi.org/10.1007/s00445-003-0277-y>

- Kilburn, C. R. (2003). Multiscale fracturing as a key to forecasting volcanic eruptions. *Journal of Volcanology and Geothermal Research*, 125(3), 271–289.
- Larsen, J. F., Neal, C., Schaefer, J., Beget, J., & Nye, C. (2007). Late Pleistocene and Holocene caldera-forming eruptions of Okmok caldera, Aleutian Islands, Alaska. In J. Eichelberger (Ed.), *Volcanism and subduction: The Kamchatka Region* (Vol. 172, pp. 343–364). Washington, DC.
- Le Mével, H., Feigl, K. L., Córdova, L., DeMets, C., & Lundgren, P. (2015). Evolution of unrest at Laguna del Maule volcanic field (Chile) from InSAR and GPS measurements, 2003 to 2014. *Geophysical Research Letters*, 42, 6590–6598. <https://doi.org/10.1002/2015GL064665>
- Lenglíné, O., Marsan, D., Got, J.-L., Pinel, V., Ferrazzini, V., & Okubo, P. G. (2008). Seismicity and deformation induced by magma accumulation at three basaltic volcanoes. *Journal of Geophysical Research*, 113, B12305. <https://doi.org/10.1029/2008JB005937>
- Lister, J. R., & Kerr, R. C. (1991). Fluid-mechanical models of crack propagation and their application to magma transport in dykes. *Journal of Geophysical Research*, 96(B6), 10,049–10,077.
- Long, S. M., & Grosfils, E. B. (2009). Modeling the effect of layered volcanic material on magma reservoir failure and associated deformation, with application to Long Valley caldera, California. *Journal of Volcanology and Geothermal Research*, 186(3), 349–360.
- López, C., Blanco, M. J., Abella, R., Brenes, B., Cabrera Rodríguez, V. M., Casas, B., ... Villasante-Marcos, V. (2012). Monitoring the volcanic unrest of El Hierro (Canary Islands) before the onset of the 2011–2012 submarine eruption. *Geophysical Research Letters*, 39, L13303. <https://doi.org/10.1029/2012GL051846>
- Lowenstern, J. B., Smith, R. B., & Hill, D. P. (2006). Monitoring super-volcanoes: Geophysical and geochemical signals at Yellowstone and other large caldera systems. *Philosophical Transactions. Series A, Mathematical, Physical, and Engineering Sciences*, 364(1845), 2055–2072.
- Lu, Z., & Dzurisin, D. (2014). InSAR imaging of Aleutian Volcanoes. In *InSAR Imaging of Aleutian Volcanoes* (pp. 87–345). Berlin: Springer.
- Lu, Z., Dzurisin, D., Biggs, J., Wicks, C., & McNutt, S. (2010). Ground surface deformation patterns, magma supply, and magma storage at Okmok volcano, Alaska, from InSAR analysis: 1. Intereruption deformation, 1997–2008. *Journal of Geophysical Research*, 115, B00802. <https://doi.org/10.1029/2009JB006969>
- Lu, Z., Mann, D., & Freymueller, J. (1998). Satellite radar interferometry measures deformation at Okmok Volcano. *Eos, Transactions American Geophysical Union*, 79(39), 466–468.
- Lu, Z., Masterlark, T., Dzurisin, D., Rykhus, R., & Wicks, C. (2003). Magma supply dynamics at Westdahl volcano, Alaska, modeled from satellite radar interferometry. *Journal of Geophysical Research*, 108(B7), 2354. <https://doi.org/10.1029/2002JB002311>
- Lu, Z., Wicks, C., Dzurisin, D., Thatcher, W., Freymueller, J. T., McNutt, S. R., & Mann, D. (2000). Aseismic inflation of Westdahl volcano, Alaska, revealed by satellite radar interferometry. *Geophysical Research Letters*, 27(11), 1567–1570.
- Lundgren, P., Usai, S., Sansosti, E., Lanari, R., Tesauro, M., Fornaro, G., & Berardino, P. (2001). Modeling surface deformation observed with synthetic aperture radar interferometry at Campi Flegrei caldera. *Journal of Geophysical Research*, 106(B9), 19,355–19,366.
- Manconi, A., Longpré, M.-A., Walter, T. R., Troll, V. R., & Hansteen, T. H. (2009). The effects of flank collapses on volcano plumbing systems. *Geology*, 37(12), 1099–1102.
- Marti, J., & Geyer, A. (2009). Central vs flank eruptions at Teide–Pico Viejo twin stratovolcanoes (Tenerife, Canary Islands). *Journal of Volcanology and Geothermal Research*, 181(1), 47–60.
- Marti, J., Pinel, V., López, C., Geyer, A., Abella, R., Tárraga, M., ... Rodríguez, C. (2013). Causes and mechanisms of the 2011–2012 El Hierro (Canary Islands) submarine eruption. *Journal of Geophysical Research: Solid Earth*, 118, 823–839. <https://doi.org/10.1002/jgrb.50087>
- Masterlark, T., Donovan, T., Feigl, K. L., Haney, M., Thurber, C. H., & Tung, S. (2016). Volcano deformation source parameters estimated from InSAR: Sensitivities to uncertainties in seismic tomography. *Journal of Geophysical Research: Solid Earth*, 121, 3002–3016. <https://doi.org/10.1002/2015JB012656>
- Masterlark, T., Haney, M., Dickinson, H., Fournier, T., & Searcy, C. (2010). Rheologic and structural controls on the deformation of Okmok volcano, Alaska: FEMs, InSAR, and ambient noise tomography. *Journal of Geophysical Research*, 115, B02409. <https://doi.org/10.1029/2009JB006324>
- McGarr, A. (1988). On the state of lithospheric stress in the absence of applied tectonic forces. *Journal of Geophysical Research*, 93(B11), 13,609–13,617.
- McLeod, P., & Tait, S. (1999). The growth of dykes from magma chambers. *Journal of Volcanology and Geothermal Research*, 92(3), 231–245.
- McNutt, S. R., & Jacob, K. H. (1986). Determination of large-scale velocity structure of the crust and upper mantle in the vicinity of Pavlof Volcano, Alaska. *Journal of Geophysical Research*, 91(B5), 5013–5022.
- McTigue, D. F. (1987). Elastic stress and deformation near a finite spherical magma body: Resolution of the point source paradox. *Journal of Geophysical Research*, 92(B12), 12,931–12,940.
- Miyagi, Y., Freymueller, J. T., Kimata, F., Sato, T., & Mann, D. (2004). Surface deformation caused by shallow magmatic activity at Okmok volcano, Alaska, detected by GPS campaigns 2000–2002. *Earth, Planets and Space*, 56(10), e29–e32.
- Mogi, K. (1958). Relations between the eruptions of various volcanoes and the deformations of the ground surfaces around them. *Bulletin of the Earthquake Research Institute, University of Tokyo*, 36, 99–134.
- Moos, D., & Zoback, M. D. (1993). State of stress in the Long Valley caldera, California. *Geology*, 21(9), 837–840.
- Moran, S. C., Newhall, C., & Roman, D. C. (2011). Failed magmatic eruptions: Late-stage cessation of magma ascent. *Bulletin of Volcanology*, 73(2), 115–122. <https://doi.org/10.1007/s00445-010-0444-x>
- Neal, C. A., McGimsey, R. G., Dixon, J., & Melnikov, D. (2005). 2004 volcanic activity in Alaska and Kamchatka: Summary of events and response of the Alaska volcano observatory. *U.S. Geological Survey, Open-File Report*, 71.
- Newhall, C. G., & Dzurisin, D. (1988). Historical unrest at large calderas of the world. *U.S. Geological Survey Bulletin*, 1109.
- Newman, A. V., Dixon, T. H., & Gourmelen, N. (2006). A four-dimensional viscoelastic deformation model for Long Valley Caldera, California, between 1995 and 2000. *Journal of Volcanology and Geothermal Research*, 150(1–3), 244–269. <https://doi.org/10.1016/j.jvolgeores.2005.07.017>
- Newman, A. V., Dixon, T. H., Ofoegbu, G. I., & Dixon, J. E. (2001). Geodetic and seismic constraints on recent activity at Long Valley Caldera, California: Evidence for viscoelastic rheology. *Journal of Volcanology and Geothermal Research*, 105(3), 183–206.
- Newman, A. V., Stiros, S., Feng, L., Psimoulis, P., Moschas, F., Saltogianni, V., ... Vamvakaris, D. (2012). Recent geodetic unrest at Santorini caldera, Greece. *Geophysical Research Letters*, 39, L06309. <https://doi.org/10.1029/2012GL051286>
- Nooner, S. L., & Chadwick, W. W. (2009). Volcanic inflation measured in the caldera of Axial Seamount: Implications for magma supply and future eruptions. *Geochemistry, Geophysics, Geosystems*, 10, Q02002. <https://doi.org/10.1029/2008GC002315>
- Okada, Y. (1985). Surface deformation due to shear and tensile faults in a half-space. *Bulletin of the Seismological Society of America*, 75(4), 1135–1154.
- Orsi, G., Civetta, L., Del Gaudio, C., De Vita, S., Di Vito, M. A., Isaia, R., ... Ricco, C. (1999). Short-term ground deformations and seismicity in the resurgent Campi Flegrei caldera (Italy): An example of active block-resurgence in a densely populated area. *Journal of Volcanology and Geothermal Research*, 91(2), 415–451.

- Pagli, C., Sigmundsson, F., Árnadóttir, T., Einarsson, P., & Sturkell, E. (2006). Deflation of the Askja volcanic system: Constraints on the deformation source from combined inversion of satellite radar interferograms and GPS measurements. *Journal of Volcanology and Geothermal Research*, 152(1–2), 97–108. <https://doi.org/10.1016/j.jvolgeores.2005.09.014>
- Parfitt, L., & Wilson, L. (2009). *Fundamentals of physical volcanology*. Oxford: John Wiley & Sons.
- Parks, M. M., Biggs, J., England, P., Mather, T. A., Nomikou, P., Palamarchouk, K., ... Zacharis, V. (2012). Evolution of Santorini volcano dominated by episodic and rapid fluxes of melt from depth. *Nature Geoscience*, 5(10), 749–754.
- Parotidis, M., Rothert, E., & Shapiro, S. A. (2003). Pore-pressure diffusion: A possible triggering mechanism for the earthquake swarms 2000 in Vogtland/NW-Bohemia, central Europe. *Geophysical Research Letters*, 30(20), 2075. <https://doi.org/10.1029/2003GL018110>
- Peltier, A., Famin, V., Bacheler, P., Cayol, V., Fukushima, Y., & Staudacher, T. (2008). Cyclic magma storages and transfers at Piton de La Fournaise volcano (La Réunion hotspot) inferred from deformation and geochemical data. *Earth and Planetary Science Letters*, 270(3), 180–188.
- Pinel, V., & Albino, F. (2013). Consequences of volcano sector collapse on magmatic storage zones: Insights from numerical modeling. *Journal of Volcanology and Geothermal Research*, 252, 29–37.
- Pinel, V., & Jaupart, C. (2000). The effect of edifice load on magma ascent beneath a volcano. *Philosophical Transactions of the Royal Society London A. Mathematical, Physical and Engineering Sciences*, 358(1770), 1515–1532.
- Pinel, V., & Jaupart, C. (2003). Magma chamber behavior beneath a volcanic edifice. *Journal of Geophysical Research*, 108(B2), 2072. <https://doi.org/10.1029/2002JB001751>
- Pinel, V., & Jaupart, C. (2004). Likelihood of basaltic eruptions as a function of volatile content and volcanic edifice size. *Journal of Volcanology and Geothermal Research*, 137(1), 201–217.
- Pinel, V., & Jaupart, C. (2005). Caldera formation by magma withdrawal from a reservoir beneath a volcanic edifice. *Earth and Planetary Science Letters*, 230(3–4), 273–287. <https://doi.org/10.1016/j.epsl.2004.11.016>
- Pinel, V., Sigmundsson, F., Sturkell, E., Geirsson, H., Einarsson, P., Gudmundsson, M. T., & Högnadóttir, T. (2007). Discriminating volcano deformation due to magma movements and variable surface loads: Application to Katla subglacial volcano, Iceland. *Geophysical Journal International*, 169(1), 325–338. <https://doi.org/10.1111/j.1365-246X.2006.03267.x>
- Pritchard, M. E., & Simons, M. (2002). A satellite geodetic survey of large-scale deformation of volcanic centres in the central Andes. *Nature*, 418(6894), 167–171.
- Pritchard, M. E., & Simons, M. (2004). An InSAR-based survey of volcanic deformation in the southern Andes. *Geophysical Research Letters*, 31, L15610. <https://doi.org/10.1029/2004GL020545>
- Reverso, T., Vandemeulebrouck, J., Jouanne, F., Pinel, V., Villemin, T., Sturkell, E., & Bascou, P. (2014). A two-magma chamber model as a source of deformation at Grímsvötn Volcano, Iceland. *Journal of Geophysical Research: Solid Earth*, 119, 4666–4683. <https://doi.org/10.1002/2013JB010569>
- Rivalta, E., Taisne, B., Bunger, A. P., & Katz, R. F. (2015). A review of mechanical models of dike propagation: Schools of thought, results and future directions. *Tectonophysics*, 638, 1–42. <https://doi.org/10.1002/2014GL060595>
- Ronchin, E., Geyer, A., & Martí, J. (2015). Evaluating topographic effects on ground deformation: Insights from finite element modeling. *Surveys in Geophysics*, 36(4), 513–548.
- Rubin, A. M. (1995). Propagation of magma-filled cracks. *Annual Review of Earth and Planetary Sciences*, 23, 287–336.
- Sammis, C. G., & Julian, B. R. (1987). Fracture instabilities accompanying dike intrusion. *Journal of Geophysical Research*, 92(B3), 2597–2605.
- Samsonov, S. V., Tiampo, K. F., Camacho, A. G., Fernández, J., & González, P. J. (2014). Spatiotemporal analysis and interpretation of 1993–2013 ground deformation at Campi Flegrei, Italy, observed by advanced DInSAR. *Geophysical Research Letters*, 41, 6101–6108. <https://doi.org/10.1002/2014GL060595>
- Sartoris, G., Pozzi, J. P., Philippe, C., & Le Moël, J. L. (1990). Mechanical stability of shallow magma chambers. *Journal of Geophysical Research*, 95(B4), 5141–5151.
- Schultz, R. A. (1995). Limits on strength and deformation properties of jointed basaltic rock masses. *Rock Mechanics and Rock Engineering*, 28(1), 1–15.
- Segall, P. (2013). Volcano deformation and eruption forecasting. *Geological Society, London, Special Publications*, 380(1), 85–106. <https://doi.org/10.1144/SP380.4>
- Segall, P. (2016). Repressurization following eruption from a magma chamber with a viscoelastic aureole. *Journal of Geophysical Research: Solid Earth*, 121, 8501–8522. <https://doi.org/10.1002/2016JB013597>
- Shapiro, S. A., Patzg, R., Rothert, E., & Rindschwendner, J. (2003). Triggering of seismicity by pore-pressure perturbations: Permeability-related signatures of the phenomenon. *Pure and Applied Geophysics*, 160(5–6), 1051–1066.
- Shibata, T., & Akita, F. (2001). Precursory changes in well water level prior to the March, 2000 eruption of Usu volcano, Japan. *Geophysical Research Letters*, 28(9), 1799–1802.
- Simakin, A. G., & Ghassemi, A. (2010). The role of magma chamber-fault interaction in caldera forming eruptions. *Bulletin of Volcanology*, 72(1), 85–101. <https://doi.org/10.1007/s00445-009-0306-6>
- Stankiewicz, J., Ryberg, T., Haberland, C., & Natawidjaja, D. (2010). Lake Toba volcano magma chamber imaged by ambient seismic noise tomography. *Geophysical Research Letters*, 37, L17306. <https://doi.org/10.1029/2010GL044211>
- Stefansson, V. (1981). *Geothermal systems: Principles and case histories* Edited by L. Rybach, & L. J. P. Muffler (pp. 273–294). New York: Wiley.
- Strehlow, K., Gottsmann, J. H., & Rust, A. C. (2015). Poroelastic responses of confined aquifers to subsurface strain and their use for volcano monitoring. *Solid Earth*, 6, 1207–1229.
- Sturkell, E., Erik, S., Páll, E., Freysteinn, S., Halldór, G., Halldór, Ó., ... Ragnar, S. (2006). Volcano geodesy and magma dynamics in Iceland. *Journal of Volcanology and Geothermal Research*, 150(1–3), 14–34. <https://doi.org/10.1016/j.jvolgeores.2005.07.010>
- Sutawidjaja, I. S., Prambada, O., & Siregar, D. A. (2013). The August 2010 phreatic eruption of Mount Sinabung, North Sumatra. *Indonesian Journal on Geoscience*, 8(1), 55–61.
- Taisne, B., Tait, S., & Jaupart, C. (2011). Conditions for the arrest of a vertical propagating dyke. *Bulletin of Volcanology*, 73(2), 191–204. <https://doi.org/10.1007/s00445-010-0440-1>
- Tait, S., Jaupart, C., & Vergniolle, S. (1989). Pressure, gas content and eruption periodicity of a shallow, crystallising magma chamber. *Earth and Planetary Science Letters*, 92(1), 107–123.
- Talwani, P., & Acree, S. (1984). Pore pressure diffusion and the mechanism of reservoir-induced seismicity. *Pure and Applied Geophysics*, 122(6), 947–965.
- Timoshenko, S., Timoshenko, S., & Goodier, J. N. (1951). *Theory of elasticity*. New York: McGraw-Hill book Company.
- Touloukian, Y. S., Judd, W. R., & Roy, R. F. (1981). *Physical properties of rocks and minerals* (Vol. 2). New York: McGraw-Hill Companies.
- Townend, J., & Zoback, M. D. (2000). How faulting keeps the crust strong. *Geology*, 28(5), 399–402.

- Trasatti, E., Casu, F., Giunchi, C., Pepe, S., Solaro, G., Tagliaventi, S., ... Lanari, R. (2008). The 2004–2006 uplift episode at Campi Flegrei caldera (Italy): Constraints from SBAS-DInSAR ENVISAT data and Bayesian source inference. *Geophysical Research Letters*, 35, L07308. <https://doi.org/10.1029/2007GL033091>
- Troise, C., De Natale, G., Pingue, F., Obrizzo, F., De Martino, P., Tammaro, U., & Boschi, E. (2007). Renewed ground uplift at Campi Flegrei caldera (Italy): New insight on magmatic processes and forecast. *Geophysical Research Letters*, 34, L03301. <https://doi.org/10.1029/2006GL028545>
- Vilardo, G., Ventura, G., Terranova, C., Matano, F., & Nardò, S. (2009). Ground deformation due to tectonic, hydrothermal, gravity, hydrogeological, and anthropic processes in the Campania Region (Southern Italy) from permanent scatterers synthetic aperture radar interferometry. *Remote Sensing of Environment*, 113(1), 197–212.
- Wagner, D., Koulakov, I., Rabbel, W., Luehr, B.-G., Wittwer, A., Kopp, H., ... Scientists, M. (2007). Joint inversion of active and passive seismic data in Central Java. *Geophysical Journal International*, 170(2), 923–932.
- Wauthier, C., Cayol, V., Kervyn, F., & d'Oreye, N. (2012). Magma sources involved in the 2002 Nyiragongo eruption, as inferred from an InSAR analysis. *Journal of Geophysical Research*, 117, B05411. <https://doi.org/10.1029/2011JB008257>
- Wauthier, C., Cayol, V., Poland, M., Kervyn, F., d'Oreye, N., Hooper, A., ... Smets, B. (2013). Nyamulagira's magma plumbing system inferred from 15 years of InSAR. *Geological Society, London, Special Publications*, 380(1), 39–65. <https://doi.org/10.1144/SP380.9>
- Wicks, C. W., Thatcher, W., Dzurisin, D., & Svart, J. (2006). Uplift, thermal unrest and magma intrusion at Yellowstone caldera. *Nature*, 440(7080), 72–75.
- Witham, C. S. (2005). Volcanic disasters and incidents: A new database. *Journal of Volcanology and Geothermal Research*, 148(3), 191–233.
- Zellmer, G. F. (2008). Some first-order observations on magma transfer from mantle wedge to upper crust at volcanic arcs. *Geological Society, London, Special Publications*, 304(1), 15–31.
- Zhao, W., Amelung, F., Doin, M.-P., Dixon, T. H., Wdowinski, S., & Lin, G. (2016). InSAR observations of lake loading at Yangzhuoyong Lake, Tibet: Constraints on crustal elasticity. *Earth and Planetary Science Letters*, 449, 240–245.
- Zimmermann, M., Prescott, M. M., & Rooper, C. N. (2016). Smooth sheet bathymetry of the Aleutian islands. US Department of Commerce, National Oceanic and Atmospheric Administration, Marine Fisheries Service, Alaska Fisheries Science Center.
- Zoback, M. D. (2010). *Reservoir geomechanics*. Cambridge, UK: Cambridge University Press.
- Zoback, M. D., & Gorelick, S. M. (2012). Earthquake triggering and large-scale geologic storage of carbon dioxide. *Proceedings of the National Academy of Sciences of the United States of America*, 109(26), 10,164–10,168.
- Zoback, M. D., & Townend, J. (2001). Implications of hydrostatic pore pressures and high crustal strength for the deformation of intraplate lithosphere. *Tectonophysics*, 336(1), 19–30.